



Mineralogy, geochemistry and monazite U-Th-Pb geochronology of the Hakimpur banded iron formation deposit, Bangladesh: a petrogenetic study

A. S. M. Mehedi Hasan^{1,2*}, I. Hossain¹, T. Tsunogae^{3,4}, M. Sahiduzzaman², Z. Yeasmin¹, M. S. Alam⁵,
M. A. Akbar⁶ and M. N. Zaman⁵

¹Department of Geology and Mining, University of Rajshahi, Rajshahi-6205, Bangladesh

²Bangladesh Petroleum Institute (BPI), Uttara Model Town, Dhaka-1230, Bangladesh

³Graduate School of Life and Environmental Sciences (Earth Evolution Sciences), University of Tsukuba, Ibaraki 305-8572, Japan

⁴Department of Geology, University of Johannesburg, Auckland Park 2006, South Africa

⁵Institute of Mining, Mineralogy and Metallurgy (IMMM), Bangladesh Council of Scientific and Industrial Research (BCSIR), Joypurhat-5900, Bangladesh

⁶Geological Survey of Bangladesh (GSB), Segunbagicha, Dhaka-1000, Bangladesh

ARTICLE INFO

Received: 06 December 2023

Revised: 14 December 2023

Accepted: 18 December 2023

eISSN 2224-7157/© 2023 The Author(s).
Published by Bangladesh Council of
Scientific and Industrial Research
(BCSIR).

This is an open access article under the
terms of the Creative Commons Non
Commercial License (CC BY-NC)
(<https://creativecommons.org/licenses/by-nc/4.0/>)

DOI: <https://doi.org/10.3329/bjsir.v58i4.70260>

ABSTRACT

The Fe-rich deposits from Hakimpur (Bangladesh) are associated with a broad range of rock types including BIF, biotite schist, quartzite and amphibolite. Geochemical analysis coupled with petrographic studies indicates the BIF and BIF-hosted rocks were derived from sedimentary protoliths. In the sediments, clay minerals were altered at a certain thermobarometric condition during metamorphism: Clay (illite) → chlorite → biotite → amphibole, which is evident from silicification, chloritization, biotitization, saussuritization and epidotization in petrographic results. Monazite chemistry U-Th-Pb geochronological evidence indicates the deposit was affected by a single, medium-grade metamorphic event that occurred at 1728 ± 28 Ma during the Basement rock's magmatic event activated. The metamorphic alteration was took place by the hydrothermal action or orogenic activity due to magmatism of Palaeoproterozoic basement rock occurred surrounding the areas. The temperatures condition and oxygen fugacities obtained from zircon and coexisting magnetite and ilmenite assemblages [$677-692^\circ\text{C}$ and $522-809^\circ\text{C}$ (at $10^{-23.9}$ to $10^{-11.9} f_{\text{O}_2}$), respectively] are partly compatible with known crystallization conditions of the dioritic basement rock in Bangladesh.

Keywords: BIF; petrogenesis; mineral chemistry; monazite geochronology; Bangladesh

Introduction

Precambrian banded iron formations (BIF) represent one of the most distinctive rock types in the world and are formed from marine chemical precipitates (Bhattacharya *et al.* 2007; Taner *et al.* 2015). They typically comprise of >15 wt.% iron with Fe-bearing minerals including primarily magnetite and minor Fe-rich carbonate (siderite) finely interlayered with iron-poor chert (Duan *et al.* 2021). According to Beukes and Gutzmer (Beukes *et al.* 2019), BIF is defined as “a variety of iron formation containing distinct finely laminated to thinly bedded chert

layers that resemble bands originated in chert-bearing chemical sedimentary rocks”. Based on thickness, BIF is primarily categorized as macrobanded (meter-thick) to mesobanded (centimeter-thick), while microbands (millimeter and sub-millimeter layers) are sometimes present and these are usually associated with episodic hydrothermal input (Konhauser *et al.* 2017). Some iron formations are known as granular iron formations (GIFs) composed of granular chert and iron oxides or silicates,

*Corresponding author's e-mail: mehedi.mpc@gmail.com

with primary diagenetic carbonate, chert or hematite cement that fill pore space (Konhauser *et al.* 2017). As a result, GIFs lack the banding feature.

Banded iron formations can be up to several hundred meters in thickness and extend laterally for several hundred kilometers. BIF-hosted Fe-rich deposits with Fe >25 wt.%, have typically been modified by diagenesis, metamorphism, and migmatization, resulting in a progressive alteration in texture and mineralogy (Klein *et al.* 2005). The upgraded deposits account for more than 60% of global iron reserves and provide most of the iron ore presently mined (Geymond *et al.* 2022). Formations can be found in Australia, Brazil, South Africa, Canada, India, Russia, Ukraine, and the United States. Banded iron formations are variously described as "itabarite" in Brazil, as "ironstone" in South Africa, and as "BHQ" (banded-hematite-quartzite) or "BSF" (banded-silica-formation) in India.

Banded iron formations are almost exclusively Precambrian in age, with most deposits dating to the late Archean (2800–2500 Ma) with a secondary peak of deposition in the Paleoproterozoic (1850 Ma) (Lambeck *et al.* 2012). Besides

their immense economic value as the world's primary source of iron and steel, their study provides insightful information regarding Earth's pre-history, in particular providing key chemical and isotopic information regarding the composition and changing nature of the Earth's hydrosphere and atmosphere as well as the evolution of the Earth's crust (Sylvestre *et al.* 2015; Soh Tamehe *et al.* 2021; Mloszewska *et al.* 2012). While there is no generally accepted classification scheme for BIF deposits, occurrences such as the Superior- and Algoma-type BIFs in North America (Zhang *et al.* 2011) mostly belong to meta-sedimentary, volcanic, sedimentary, complex and magmatic types (Liu *et al.* 2014). Characteristically the Algoma-types are associated with volcanic rocks deposited in deep-water in the sequence of Archean greenstone belts, whereas the Superior-types are strata-bound in fine-grained sedimentary sequences extend over passive continental margins (Zhai *et al.* 2011; Zhai *et al.* 2013).

Occurrences of metamorphosed BIF and BSF exist widely in the East Indian shield, which includes parts of the states of Bihar, Jharkand, Uttar Pradesh, Odisha and West Bengal. The iron ore deposits in eastern India near Dinajpur, Bangladesh (Fig. 1) (Jones *et al.* 1934) are considered to be of volca-

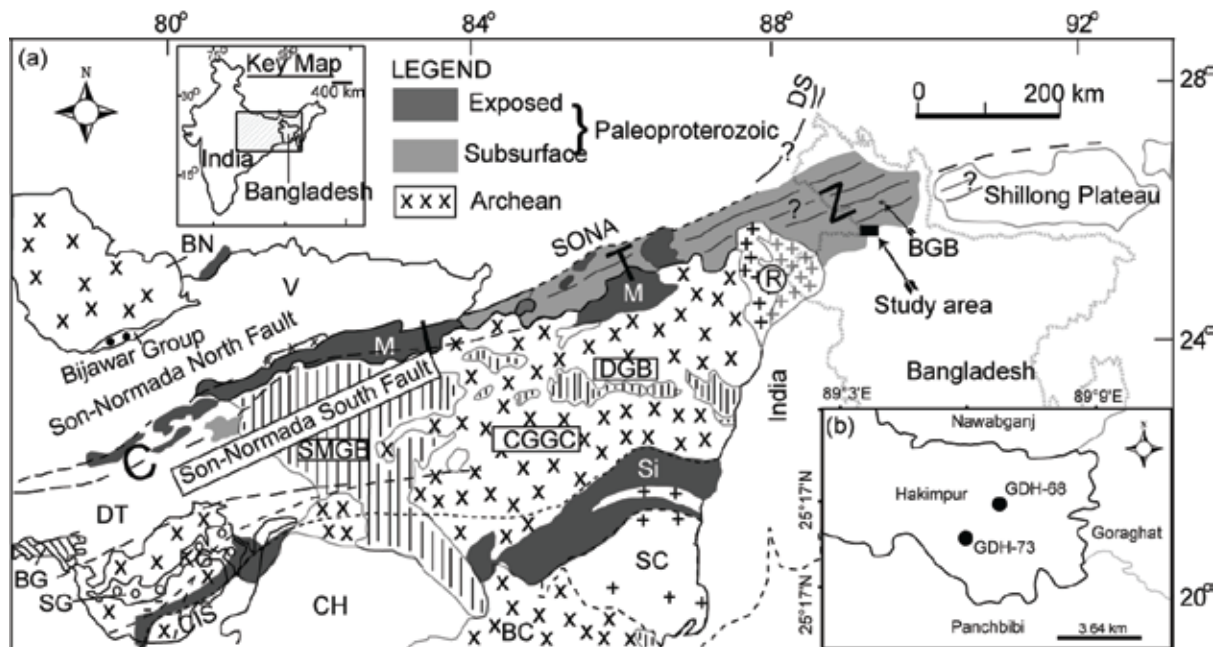


Fig. 1. (a) Location map of the Hakimpur banded iron formation deposits in Bangladesh, showing the various lithological units and tectonic features of the Central Indian Tectonic Zone (CITZ) (Hossain *et al.* 2018). Here, BGB- Barapukuria Gondwana Basin, BN- Bundhelkhand Craton, BC- Bastar Craton, BG- Betul Group, CGGC- Chotanagpur Granite Gneiss Complex, CIS- Central Indian Shear Zone, CH- Chattisgarh, DS- Darjeeling-Sikkim Himalaya, DT- Deccan Trap, DGB- Damodar Gondwana Basins, KG- Karimnagar Granulite Belt, M- Mohakoshal and equivalents, R- Rajmahal Trap, SC- Singhbhum Craton, SG- Sausar Group, SMGB- Son Mahanadi Gondwana Basins, SONA- Son Narmada Lineament, Si- Singhbhum (Paleoproterozoic), V- Vindhyan. (b) The studied boreholes (GDH-68 and GDH-73) in the Hakimpur in Dinajpur District are indicated

no-sedimentary origin and recently, ironstone deposits have been discovered in Hakimpur (Dinajpur district), Bangladesh by the Geological Survey of Bangladesh (GSB). The region contains the first-ever significant BIF iron ore accumulation discovered in Bangladesh occurring as a 122 m thick iron-rich layer at a depth of 405 m below surface and extending over an area of 6–10 km² (Angerer *et al.* 2015). This paper presents the first whole-rock geochemistry, individual BIF-hosted mineral (e.g. Fe-Ti oxide minerals, zircon, and monazite) geochemistry and geochronology of U-Th-Pb_{total} monazite sourced from well-preserved samples of the Hakimpur BIFs recovered from diamond drillcores. The new results aim to constrain the genesis and depositional age of the studied BIFs as well as the tectonic environment from which the BIFs were derived to provide an improved understanding of BIF genesis in Bangladesh.

Geological setting

Bangladesh lies in the northwest corner of the Indian subcontinent at the head of the Bay of Bengal occupying the major part of the Ganges-Brahmaputra delta, the largest of its kind in the world in terms of sediment load carried to the ocean (Orton *et al.* 1993). The geological evolution of the Bengal Basin is related to the uplift of Himalayan Mountain ranges to the north and northwest and the subsequent outbuilding of a large deltaic landmass by the major Ganges-Brahmaputra river systems originating from the uplifted Himalaya.

The long-lasting super-continental frameworks of the Columbia and Gondwana disruption was first triggered by a large mantle plume associated with the Kerguelen hotspot, which is thought to have started seafloor spreading between India and Antarctica about 132 million years ago (Davis *et al.* 2016). Subsequently, the Rajmahal-Sylhet Traps formed from a single eruption with a very large diameter approximately 117–118 Ma ago (Baksi *et al.* 1995; Ray *et al.* 2005; Talwani *et al.* 2016). The Bengal Basin was formed by the collision of the Indian and Asian plates. The northwestern part of Bangladesh (Bogra-Rangpur-Dinajpur area) was originally connected to Antarctica, Australia and other countries along with the Indian landmass, forming the Gondwana supercontinent in the southern hemisphere. About 110 Ma ago, during the Cretaceous, the Gondwana supercontinent began to breakup and India drifted north resulting in collision between the Indian plate and the Asian plate. The collision took place in stages beginning in the Eocene (55 Ma), when initial uplift to produce a proto-Himalayan range occurred (Molnar *et al.* 1975; Molnar *et al.* 1977; Curray *et al.* 1982). By the late Eocene (40 Ma), the last remnant of the Tethys sea between the Indian and Asian plates disappeared and the newly formed depression was accompanied by further rise of the Himalayan mountain range in the north.

Tectonically Bangladesh is divided into two major units: (i) Stable Precambrian Platform in the northwest and (ii) Geosynclinal basin in the southeast. A narrow northeast-southwest trending Hinge Zone separates the two above mentioned units almost in the middle of the country. The iron ore deposit in Hakimpur is located on the Rangpur Platform/Saddle (Dinajpur Slope) which forms the eastern continuation of the Indian Shield as well as part of the stable platform in northwestern Bangladesh. The Rangpur saddle formed in the hinge zone of the basin or the basinward extension of the stable shelf. It is composed of continental crust overlain by Cretaceous (144 to 66 Ma) to Recent sediments. The stratigraphic sequence of the Rangpur Saddle has been established based on subsurface drilling and geophysical data. Outside the basin area, the crystalline basement is directly superimposed by Tertiary sediments (Miah *et al.* 2002). The crystalline basement rocks (Paleoproterozoic) in the sampling area are unconformably covered by a thin sedimentary formation of Permian (Lopingian) Gondwana fluvial sediments and Cretaceous to Pleistocene sedimentary sequences exists with Recent alluvial cover (Hossain *et al.* 2013).

Sampling

Two drill cores, GDH-73 and GDH-68 were examined for this study. The locations of the two cores are shown in Fig. 1, while detailed stratigraphic columns showing the lithological units are provided in Fig. 2. Upper units consisted of Cenozoic age sediments with the youngest being the Pleistocene Barind clay unit comprising red soils dominated by clay minerals including kaolinite, illite and chrysotile (Aftabuzzaman *et al.* 2013). Beneath the Barind clay, the Dupi Tila formation is composed of yellow to light brown, medium to very fine, moderately hard to loose sandstone, siltstone, silty clay, mudstone and shale with some conglomerates with clasts of petrified wood. This unit represents the fluvial plain deposition, following the delta filling of the basin. The next oldest unit is the Jamalganj formation and consists of deltaic sandstone, shale and siltstone, which is above the Kopili formation, and composed of dark grey to black fossiliferous shale with a few limestone beds. The Kopili formation unit marks the end of open marine conditions of deposition (Alam *et al.* 2009). The oldest Cenozoic unit is the Tura formation. The lithology consists of sandstone with subordinate shale and marl with occasional carbonaceous shale. The sandstone is light grey, white, dirty white and light brown and is fine to coarse-grained and even pebbly in places (Howladar *et al.* 2018).

The basement was reached at a depth of ~398–403 m in both drill cores. The basement was characterized by a well-defined weathering layer representing an unconformity. In both cores, the main iron-bearing units were immediately present

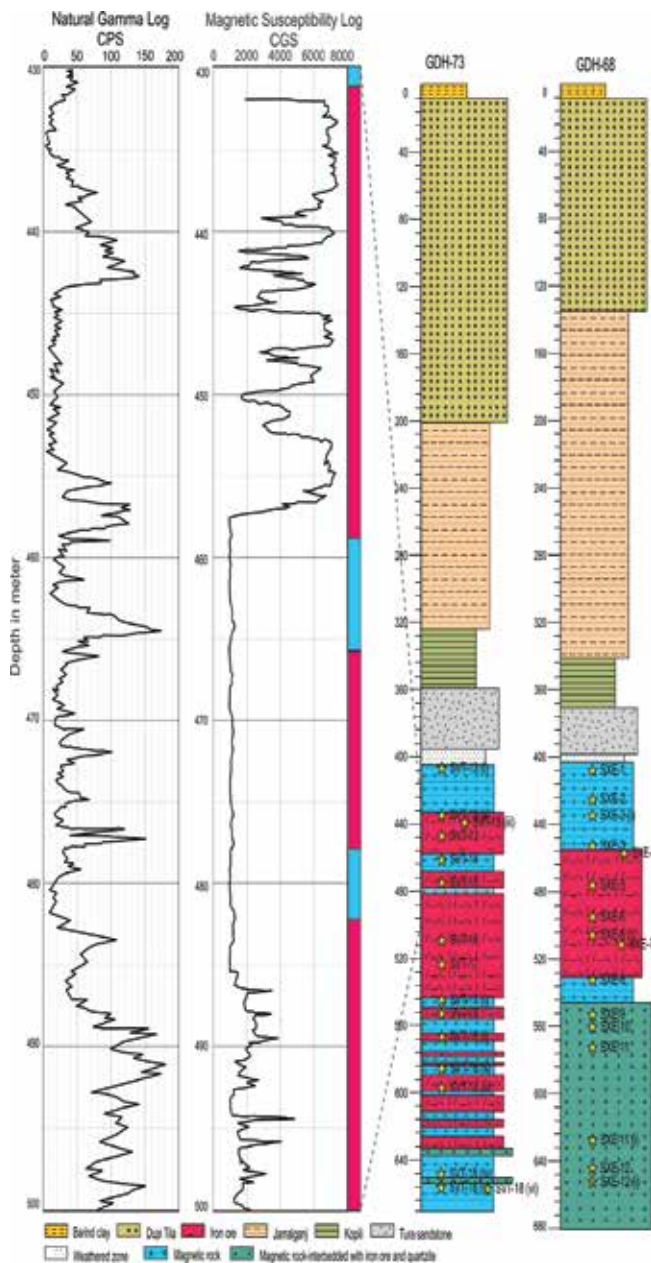


Fig. 2. Stratigraphic columns with natural gamma log and magnetic susceptibility log data for drillholes GDH-68 (right) and GDH-73 (left) of the Hakimpur iron deposit (modified after GSB, 2020). The borehole data represents the stratigraphic correlation and the variation in rock types with depth

below the weathered zone at depths greater than about 403–450 m (Fig. 2). At the top of each unit was a zone of ~27–50 m thick of magnetic rock consisting amphibolite and biotite schist, which was immediately underlain by the main

iron-bearing units occurring as a large continuous ~60–80 m sequence in GDH-68 and as an ~200 m thick sequence of iron-bearing units interbedded with series of thin layers comprising amphibolite, biotite schist and quartzite in GDH-73 (Fig. 2).

A natural gamma log of core GDH-73 was recorded from 435 to 503 m depth, corresponding to a section of the main iron-bearing unit (Fig. 2). No significant variation in signal intensity (intensities ranged between 4 and 138 cps) was observed within this depth, although few distinct zones of alternative high and low peaks were present. These may be associated with a fracture zone known to be present within the region (GSB). The natural gamma log at this depth in GDH-68 also showed a similar result.

A magnetic susceptibility log of core GDH-73 was performed within the same interval as the natural gamma log. Results are provided in Fig. 2. The magnetic susceptibility log values indicate the main iron-bearing unit consists of three distinct zones. Zone-1 (432–457 m) is a high magnetic susceptibility zone with values ranging from 1300 to 7464 cgs (5596 cgs on average), which indicates the enrichment of magnetic minerals in the host rock. Zone-2 (458–488 m), a region where the magnetic susceptibility ranges from 959 to 2757 cgs (1104 cgs on average) indicating a low proportion of magnetic minerals are present. This corresponds to a zone where there are a higher proportion of chert-like layers in the core. Likewise, for Zone-3 (489–503 m), the magnetic susceptibility values range from 1026 to 5053 cgs (2053 cgs on average) indicating moderate enrichment of magnetic minerals.

Materials and method

Whole rock geochemistry

Two drill cores (GDH-68 and GDH-73) were examined in this study. Representative rock types from different depths in the core (samples labelled SXE 1–5, 7 are from GDH-68 and samples SVT 13, 15, 16 are from GDH-73) were sampled and sectioned into smaller pieces to analyze mineralogical (optical microscopy, electron diffraction) and geochemical variability. Depths and lithological units from which the samples were taken are shown in Fig. 2.

Geochemical analysis of nine samples was conducted on a Rigaku ZSX Primus XRF (x-ray fluorescence spectroscopy) system at the Institute of Mining, Mineralogy and Metallurgy (IMMM), BCSIR, Bangladesh. In order to have precise homogeneity, the glass fusion bead method was used instead of the pressed powder pellet method, since difficulties may arise in preparing calibration standards because of its less

homogeneity (Nakayama and Nakamura, 2005). Glass fusion beads were prepared through the mixing of alkali flux i.e., lithium tetraborate ($\text{Li}_2\text{B}_4\text{O}_7$) and lithium metaborate (LiBO_2) at 80% and 20% respectively. Sample to flux ratio was remained 1:2 during heating in a high-frequency automatic bead sampler (Tokyo Kagaku Co. Ltd.). According to Nakayama and Nakamura (2005), this flux ratio improves the accuracy and sensitivity of the elements from dilution glass beds, in turn, gives better results compared to the conventional sample made with a flux ratio of 1:10. In this study, stream sediments (JSD 1, JSD 2, and JSD 3) obtained from Geological Survey of Japan (GSJ) and USGS rock standards (AVG 2, BCR 2, BHVO 2, BIR 1, and GSP 2) were used as the calibration standard aiming to validate the analytical database. Noteworthy, the analytical uncertainties for major elements were 1–5%.

XRD analysis

XRD patterns were recorded on micronized (<5 μm) samples using a Panalytical XPERT-PRO (PW3040/60), Netherlands diffractometer using $\text{Cu-K}\alpha$ radiation generated at 40 kV and 30 mA. The diffractometer was equipped with a 1.52 mm divergence slit and 0.5 mm receiving slit, a secondary monochromator, a solid-state detector and a sample changer (sample diameter 16 mm). Samples were analyzed from 5° to 70° 2θ with a step size of 0.02° 2θ and a scan speed of 1.5° $2\theta/\text{min}$, with the measurement time being 1 s per step. The top-loading technique was used for the sample preparation.

Samples were run on the diffractometer three times. The first run used untreated or air-dried samples. Samples containing ethylene glycol were used in the second run. Ethylene glycol was used to expand swelling clays, and whether or not a clay mineral expands, and the amount of expansion, can provide essential supplementary information aiding clay-mineral identification. Swelling clays include smectites (e.g., montmorillonite, nontronite, and beidellite), some mixed-layer clays, and vermiculite. In the third run, the samples were heated at 550°C for 1.5 hours. This triplicate procedure was used because the existence of some clay minerals in BIFs may have similar lattice structures (as indicated by similar diffractogram patterns) that can react differently to glycolisation and heating. In our sample, glycolisation did not affect the x-ray diffraction patterns indicating that swelling clays were not present.

Monazite chemistry for geochronology

The geochronology of the sample SXE-3 was obtained using Th-U-Pb (total) monazite dating utilizing monazite grains from textural associations within the mineral assemblages in the representative BIF and BIF hosted rocks from Hakimpur. The polished thin section of the sample was used for the

petrographic study, utilizing wavelength dispersive spectrometry with an electron microprobe analyzer (JEOL JXA8530F Hyperprobe) at the Chemical Analysis Division of the Research Facility Center for Science and Technology, University of Tsukuba. The analysis was performed with 20 kV accelerating voltage and 50 nA beam currents for the monazites and 10 nA for the standard materials, and utilizing a beam diameter of three microns. The raw data were processed using an oxide ZAF correction program supplied by JEOL. The standard materials for quantitative analyses of the monazites were synthetic glass for Pb ($\text{PbO} = 21.9 \text{ wt.}\%$), metallic uranium for U, endmember synthetic ultraphosphates (XP_5O_{14}) for the REE (La, Ce, Pr, Nd, and Sm) and Y, $\text{CeP}_5\text{O}_{14}$ for P, and wollastonite for Ca and Si. The X-ray lines were U-M β , Pb-M β , Th-M α , P-K α , Si-K α , Ca-K α , Nd-L α , Sm-L α , Ce-L α , La-L α , Pr-L α , and Y-L α .

Mineral chemistry

The compositions of key minerals including Fe-Ti oxide minerals and zircon were obtained by Field Emission Scanning Electron Microscopy (ZEISS Gemini Sigma FE-SEM 300) at IMMM, Bangladesh. The geochemical data set for minerals was obtained employing two different methods involving element mapping and quantitative analysis. FE-SEM mapping was fixed with the operating conditions of 20 kV accelerating voltage. ED and WD signals both were measured simultaneously at each step in the map to confirm the chemistry of phases. WD detector was equipped with thallium hydrogen phthalate (TAP) and pentaerythritol (PET) crystals. For analyzing the elemental suits of Si, Ti, Al, Fe, Mn, Mg, Ca, Na, K and Zr, the calibration standards including albite ($\text{NaAlSi}_3\text{O}_8$), orthoclase (KAlSi_3O_8), calcite (CaCO_3), forsterite (Mg_2SiO_4), rhodonite (MnSiO_3), hematite (Fe_2O_3), rutile (TiO_2) and zircon (ZrSiO_4) were used. Mentioning, the standard library was generated from 32mm (dia.) x 5mm brass mount mineral standards manufactured by MAC (serial number 14172). The detection limits (in ppm) were in the range of Si (500), Ti (350), Al (300), Fe (450), Mn (250), Mg (250), Ca (100), Na (450), K (100) and Zr (420), while the concentration of oxygen was calculated based on valence difference. Elemental analyses were corrected for atomic number (Z), absorption (A) and fluorescence (F) using the $\phi\rho z$ (Phi-Rho-Z) procedure. In addition, the temperature and oxygen fugacity of co-existing Fe-Ti oxide minerals were calculated using ILMAT, a magnetite-ilmenite geothermobarometry program (version 1.20) developed by Lepage *et al.* (2003).

Results

Petrography

Thin sections were prepared for all nine samples (SXE 1–5, 7 and SVT 13, 15, 16) for detailed petrographic examination. In general, the samples showed considerable textural and mineralogical variation ranging from a coarse-grained

porphyroblastic texture exhibiting significant deformational features due to metamorphism (e.g., SXE 1–5, 7 and SVT-15) through to a schistose texture (e.g., SXE 2, 5 and 7) characterized by a fine to medium grained minerals chiefly of biotite-rich platy minerals. Based on texture, metamorphic fabrics and mineral assemblages, the studied rocks have been classified as BIF (banded iron formation), biotite schist, amphibolite and quartzite. Each of these rock types is

Table I. Modal compositions (%) of the selected rock samples from Hakimpur BIF deposits in Bangladesh

Mineral	Opq	Cal	Sd	Grt	Qtz	Pl	Or	Ep	Hbl	Bt	Chl	Mc	Py	Ilm	Ap	Zrn	Tur	Rock Type
SXE 01	34.7	9.7	21.5	8.2	23.2									2.8				BIF
SXE 02	2.0				13.8	19.0	6.7	4.0	41.5	10.0		1.0			1.3	0.5	0.2	Amphibolite
SXE 03	9.3	1.3			62.3	5.2	3.2	1.8		10.7	5.5			0.7				Biotite schist
SXE 04	4.2	2.7			71.2	4.5	0.8	0.7		13.0	1.7				0.8	0.3	0.2	Quartzite
SXE 05	2.2				9.7	18.0	2.3	0.2	56.2	8.2			0.8		1.3	0.7	0.5	Amphibolite
SXE 07	4.0				3.7	7.5	12.3	1.5	49.8	19.5					1.2	0.3	0.2	Amphibolite
SVT-13	10.8	2.8	3.5	1.3	32.3	3.3	1.7	0.5		36.0	7.3			0.5	0.8			Biotite schist
SVT-15	44.8	10.7	15.3	5.6	20.4									3.2				BIF
SVT-16	7.1	1.1	2.7	1.5	47.8	3.3	2.5	1.2		23.4	6.4			2.5	0.8			Biotite schist

Here, Opq- opaque, Cal- calcite, Sd- siderite, Grt- garnet, Qtz- quartz, Pl- plagioclase, Or- orthoclase, Ep- epidote, Hbl- hornblende, Bt- biotite, Chl- chlorite, Mc- microcline, Py- pyrite, Ilm- ilmenite, Ap- apatite, Zrn- zircon, Tur- turmaline

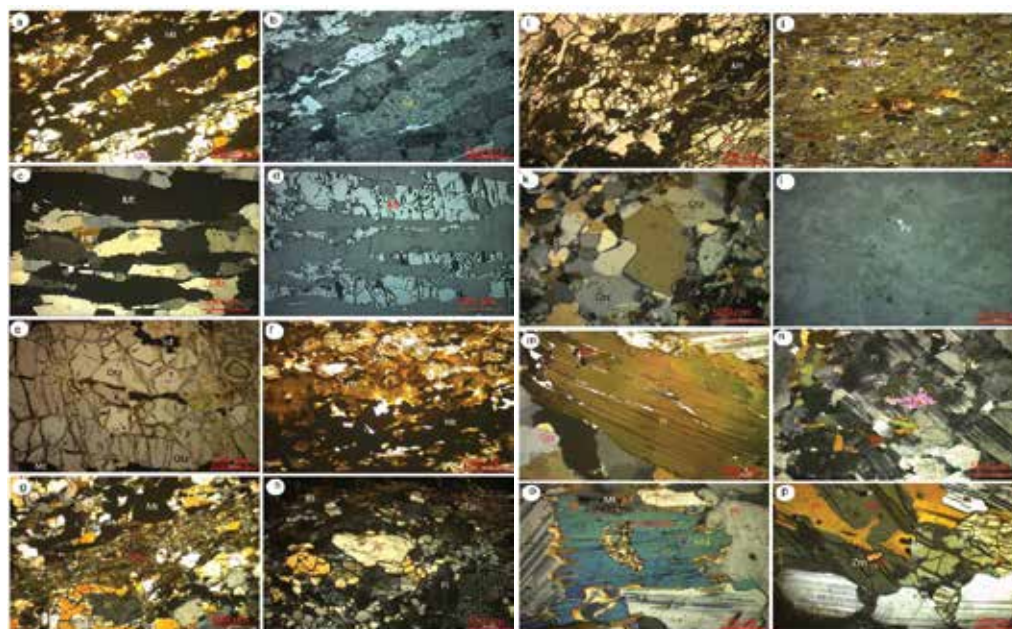


Fig. 3. Petrographic microphotographs of the studied rocks. (a–f) display hand specimen of BIFs (SXE-1 and SVT-15), where thinly bedded or laminated hematite/limonite exists with the layers of quartz, chert, siderite and calcite. Overgrowth of quartz surrounding the boundaries observed in BIF and BIF-hosted rocks (c, e, k). Gt- goethite, Mt- magnetite, Sd- siderite, Qtz- quartz, Py- pyrite, Cal- calcite, Bt- biotite, Pl- plagioclase, Ep- epidote, Chl- chlorite, Ser- sericite, Hbl- hornblende and Zrn- zircon, Fb- fossil boundary. Magnetite and pyrite show a bright white color in reflected light (b), (d) and (l). BIF (a–f), biotite schist (g–j), quartzite (k–m), and amphibolite (n–p)

discussed separately, below and modal compositions showing the proportions of different minerals in each sample are provided in Table I. The modal composition of rock types was determined by using a percentage counting technique on a grid pattern and results are expressed in percentage.

BIF (Banded iron formation)

Examination of samples SXE-1 and SVT-15 shows a thinly bedded or laminated structure comprising magnetite and hematite mixed with fine-grained limonite (possibly goethite) which comprises 35–45% of the sample. The Fe-rich oxides/oxyhydroxides are accompanied quartz (20.4–23.2%), siderite and calcite with minor chlorite, plagioclase and hornblende (Fig. 3a–d,f). The BIF samples characteristically show a coarse-grained, porphyroblastic, texture and exhibit preferred orientation in the form of banding. The BIF is generally characterized by intercalated quartz and magnetite/hematite/limonite-rich dark bands, where minerals such as siderite and a goethite-rich yellowish-red layer often occur between the Fe-rich layers, conveying a reddish coloration to the BIFs. In regions dominated by quartz and magnetite bands, the magnetite grains are subhedral to euhedral in shape and may be distributed uniformly or interconnected, forming larger aggregates. Grain boundaries that are shared with other minerals are generally straight to smoothly curved. Goethite veins are developed when a crack is formed (Fig. 3a) allowing fluids to alter the primary magnetite/hematite. Fine- to medium-grained siderite crystals are also present, existing as subhedral rhomboids and sometimes showing the development of rims, although the edges often show corrosion cracks that have a clear core and terminus with bright rims of uniform thickness that retain Fe-enrichment. Quartz is intermixed with magnetite and goethite, and many quartz grains display an inequigranular texture, evident through undulose extinction. Samples (i.e., SXE-1 and 7) obtained from the vicinity of faults show a partially cemented fracture network. Cementation in the fractures shows quartz present as overgrowths on original quartz detrital grains along the fracture plane (Fig. 3c, e, k). Also in these regions, intergranular siderite cement is encased with euhedral faces of formerly crystallized quartz. In general, mineral cements contain calcite and silica phases such as iron oxides.

In the studied borehole, the sample SXE-1 consists mainly of hematite and limonite iron-rich minerals as observed from hand specimen and high loss on ignition (LOI 9.94 wt.%), although in XRD Fig. S1 shows goethite. It happens because limonite is not a true mineral but a mixture of similar hydrated iron oxide minerals that are mostly made up of goethite, therefore massive goethite and limonite can be indistinguish-

able (Bustamante *et al.* 2006). On the other hand, XRD Fig. S1 for the sample SVT-15 displays, it consists chiefly of goethite and magnetite. Noteworthy, the negative LOI (-0.65 wt.%) of this sample indicates a phase transformation associated with the oxidation of ferrous iron (Fe^{2+}) to ferric iron (Fe^{3+}) has taken place during ignition in goethite (Vandenbergh *et al.* 2010).

Biotite schist

In the studied boreholes, biotite schists were present as evidenced by examination of samples SXE-3, SVT-13, and SVT-16. These samples are principally consisted of biotite, quartz, chlorite, orthoclase, plagioclase, epidote, calcite, apatite, and opaque minerals such as siderite, goethite, ilmenite, magnetite (Table I). The mineral assemblages of these rocks are very similar in microstructure and mineralogy (Fig. 3g–j) and are characteristically porphyroblastic, medium- to coarse-grained in texture, and showing strong evidence of preferred orientation. The grain boundaries of plagioclase grains are conspicuously ragged and indented due to these sites being the preferred locations for the initiation of corrosion and the precipitation of new phases. During alteration during metamorphism, silicification has occurred and a silica cement is now present, and this binds the quartz grains in place. In contrast, chlorite is formed because of hydrothermal alteration.

Generally, schistose texture and in some cases local crenulation cleavages are present in the biotites resulting in the formation of superimposed foliations. The core of the deposit has undergone biotite-rich alteration peripherally (without K-feldspar) in wall rocks, as well as propylitic alteration zones containing epidote. Likewise, epidotization and sericitization are most common in the studied biotite schist (Fig. 3h and 3j respectively).

Calcite occurs in association with siderite and minor hematite, but pure silica is also observed among the Fe-oxide microlaminates. Hematite, magnetite, and siderite usually contain inclusions of chert, which becomes trapped during crystal growth or due to the coalescence of Fe-oxide-rich microlayers. In addition, chertification in the sample has occurred (Fig. 3g), when chert as silicon dioxide grows within soft sediments that are chemically precipitated in the sedimentary rock (Boggs, 2012; Blat *et al.* 2006).

Quartzite

Quartzite is a hard, non-foliated metamorphic rock. In the studied boreholes, the mineral assemblages present in sample SXE-4 are chiefly quartz (71%) and others (e.g., plagioclase, orthoclase, biotite, chlorite, epidote, opaque, calcite, siderite,

zircon, apatite, and tourmaline) (Table I). The sample displays a very coarse-grained, not preferred oriented (massive), porphyroblastic texture. Quartz shows granoblastic polygonal (Fig. 3k), where the equidimensional grains have developed crystal faces resulting in straight grain boundaries, and well-defined triple junctions are common. Fe-rich layers are also present, and these display many cracks in which magnetite is often partially replaced by pyrite (Fig. 3l). Here, chertification is evident and primary-level plagioclase feldspar grains are present (Fig. 3m). Prograde metamorphism, sericitization in plagioclase feldspar and biotitization are also visible in Fig. 3m.

Amphibolite

Mineral assemblage in samples SXE-2, SXE-5 and SXE-7 are mostly composed of amphibole (primarily hornblende at 41–50%) and plagioclase, with variable amounts of quartz, epidote, biotite, orthoclase, microcline, apatite, zircon, tourmaline and opaque minerals (e.g. pyrite, magnetite and hematite). The studied amphibolites show a very coarse-grained texture, a non-preferred orientation (massive), and porphyroblastic texture. Thin section studies indicate they are more cracked, which presumably occurred before alteration. Biotitization induces hornblende to be altered into biotite (Fig. 3n-p), whereas saussuritization is formed where plagioclase feldspar is altered into epidote by the replacement of K-feldspar (Fig. 3n). Epidote is identified by yellowish green color, one set of perfect cleavages, a refractive index high, interference color low second order to upper third order. Zircon metamictization is also visible (Fig. 3p).

Whole rock geochemistry

The nine drilled core rock samples were analyzed for major oxides and the results are listed in Table II.

Major oxides

The rock samples had variable content of SiO₂ contents extending from 18.34 wt.% in the BIF samples (SXE-1 and SVT-15) to 55.35 wt.% in biotite-schist (SVT-1). The biotite schist, amphibolite and quartzite samples all had relatively high Al₂O₃ contents (15.24–18.99 wt.%), whereas the two BIF samples were low in Al₂O₃ (both ~1.05 wt.% Al₂O₃) consistent with mineralogy dominated by Fe-oxides and oxyhydroxides and quartz. All samples had moderate compositions of alkalis with K₂O ranging from 0.01 wt.% (BIF) to 5.51 wt.% (quartzite), while Na₂O ranged from 0.07 to 2.67 wt.%. The Fe₂O₃(T) contents ranged from a minimum of 13.83 wt.% in the biotite-schists to a maximum of 76.44 wt.% in the BIF. The TiO₂ contents were relatively low in all samples, with the lowest at 0.05 wt.% for the BIF to a high of 2.11 wt.% for the quartzites. All the major elements of the BIF hosted rocks exhibit decreasing Fe₂O₃(T) (r = -0.95) contents with increasing SiO₂, whereas Al₂O₃ (r = 0.86), TiO₂ (r = 0.67), MnO (r = 0.52), MgO (r = 0.58), CaO (r = 0.43), Na₂O (r = 0.69) and K₂O (r = 0.69) all broadly increased with Fe₂O₃(T) (Fig. 4). These variations are compatible with the mineral compositions, suggesting that these elements were not significantly altered during later metamorphism (Dan *et al.* 2012) or hydrothermal modification (Dai Yanpei *et al.* 2012).

Mineral chemistry of Fe-Ti Oxides

A thin section was prepared from SVT-16 rock sample for a detailed petrogenetic study of Fe-Ti oxide minerals because of its dominancy. From ore microscopic observation, it is obvious the coexistence of magnetite/titanomagnetite with ilmenite was hardly preserved in other studied samples. Following accepted definitions for Fe-Ti oxides, exsolved and intergrowth phases in solid solution are collectively described as exsolution/intergrowth lamellae (Haggerty

Table II. Major element abundances of the selected rock samples from Hakimpur BIF deposits in Bangladesh

Oxide in wt. %	SXE-1 BIF	SXE-02 Amphibolite	SXE-03 Biotite schist	SXE-04 Quartzite	SXE-05 Amphibolite	SXE-07 Amphibolite	SVT-13 Biotite schist	SVT-15 BIF	SVT-16 Biotite schist
SiO ₂	18.34	45.60	46.44	46.19	40.85	42.71	55.35	26.02	40.50
Al ₂ O ₃	1.08	15.68	17.88	15.24	17.19	16.57	15.69	1.03	18.99
Fe ₂ O ₃ (T)	76.44	17.72	13.83	14.95	20.24	16.97	14.48	66.15	23.26
MnO	0.17	0.34	0.24	0.24	0.34	0.32	0.24	0.12	0.15
MgO	1.00	3.48	3.58	6.85	3.55	5.50	2.69	1.17	4.98
CaO	1.91	11.21	11.33	5.76	12.10	12.88	3.72	3.53	3.75
Na ₂ O	0.07	1.65	2.52	0.44	1.72	1.91	2.13	0.10	2.67
K ₂ O	0.01	1.87	1.78	5.51	1.35	0.97	3.99	0.06	3.69
TiO ₂	0.05	1.11	0.90	2.11	1.23	0.94	0.96	0.23	1.53
P ₂ O ₅	0.18	0.34	0.35	1.51	0.51	0.48	0.12	1.13	0.18
Total	99.24	99.01	98.86	98.81	99.08	99.27	99.37	99.54	99.70

2018). Results from the textural analysis of the Fe-Ti oxides indicate that there is no exsolution/intergrowth lamella in the crystalline phases (Fig. 4). The homogenous phases are dominantly magnetite/titanomagnetite (ave. 75%) with minor ilmenite (ave. 24%) and rare rutile and chromite (ave. 1%). The most common Fe-Ti oxides in the studied formation show sandwich-type texture and representative images of the Fe-Ti oxide phases are provided in Fig. 5.

The compositions of ilmenite are presented in Supp. Table I. As electron beam methods are unable to distinguish between Fe^{3+} and Fe^{2+} , all iron present is expressed as FeO(T) (Supp. Table I). Redistribution of FeO and Fe_2O_3 in ilmenite is based on the charge balance and stoichiometry of ilmenite and magnetite, respectively, using the method of LePage (2003). The results indicate that the host ilmenite has TiO_2 contents ranging from 31.89–50.69 wt.%. These numbers are

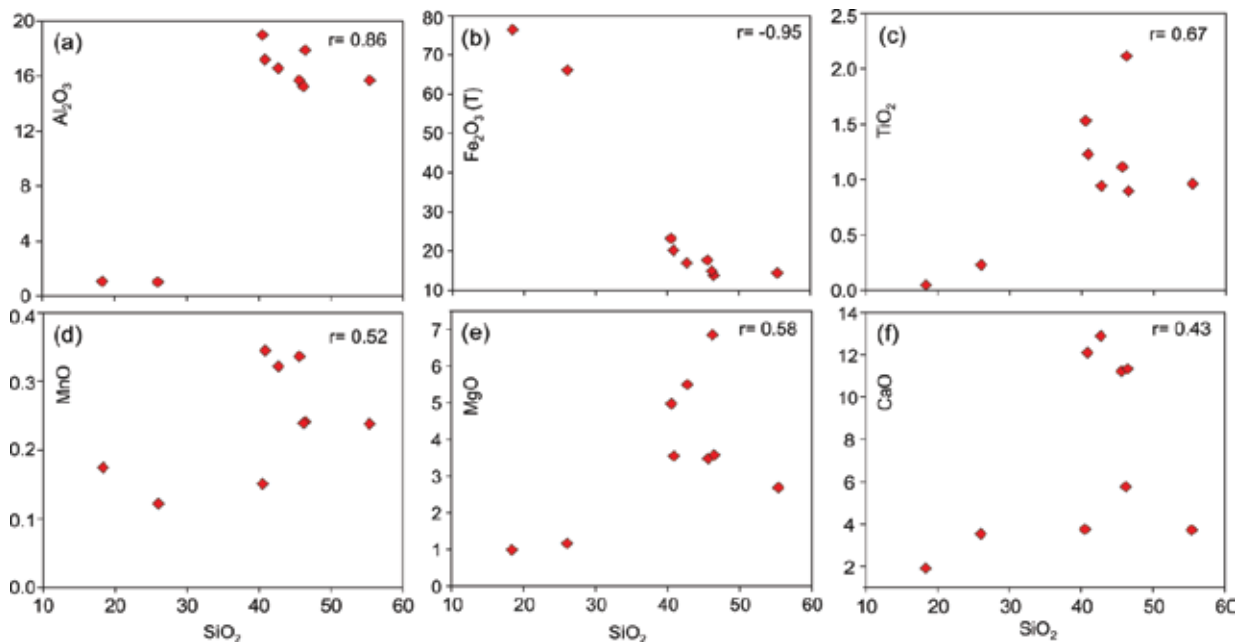


Fig. 4. Harker variation diagrams for representative major elements (wt.%) of the Hakimpur BIF and BIF hosted rocks in Bangladesh

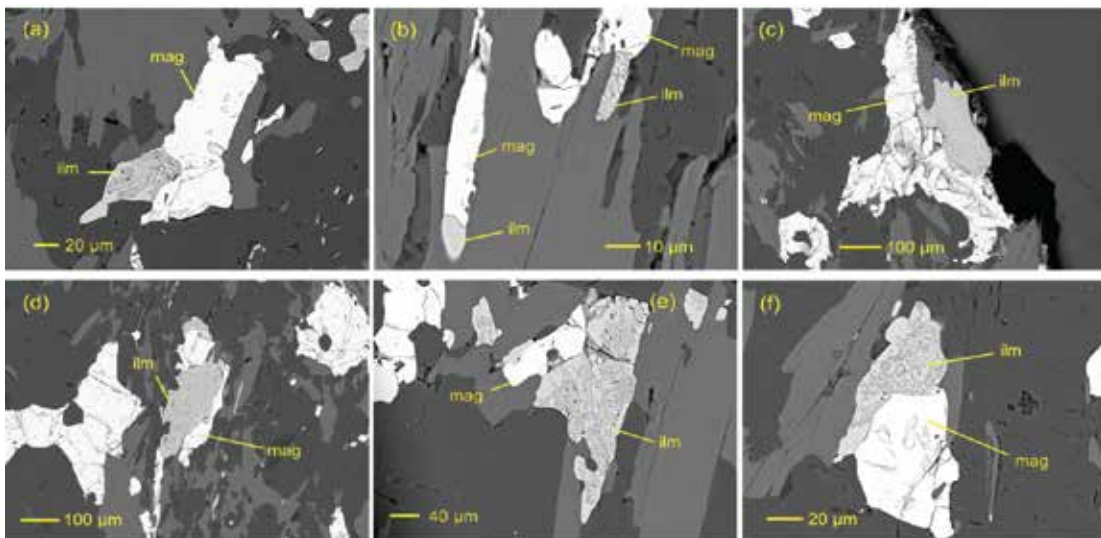


Fig. 5. Back-scattered electron (BSE) images of Fe-Ti oxide minerals in sample SVT-16 (borehole GDH-73). Different magnifications of the image are due to the small size of the grains

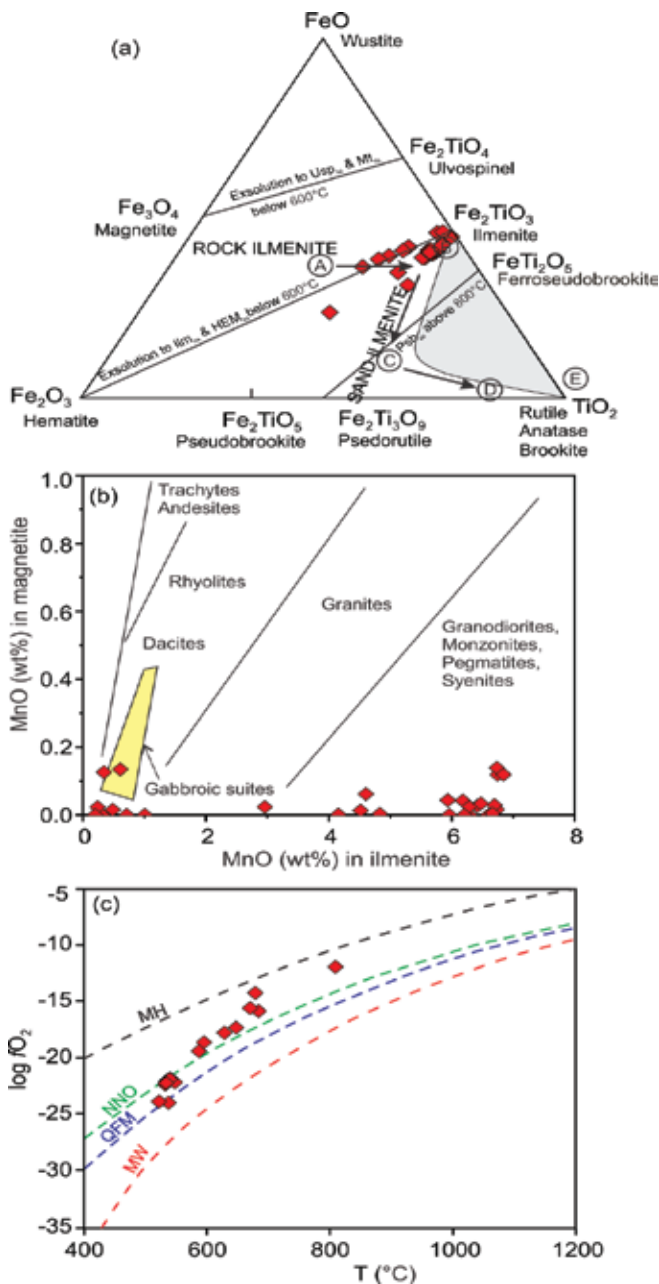


Fig. 6. The diagram illustrates the equivalent nature of igneous rock type (Reynolds, 1983), aiming to understand the protolith (a) The general distribution of Mn in Mtss and Ilmss as a function of defining rock type. (b) Plots of oxygen fugacity vs. temperature of coexisting magnetite-ilmenite pairs (Buddington *et al.* 1964). (In Fig., MH- magnetite-hematite; NNO- nickel-nickel oxide; FMQ- fayalite-magnetite-quartz; WM- wüstite-magnetite). (c) Solid phases occurring in the ternary system of FeO–Fe₂O₃–TiO₂. The compositions of the ilmenites are plotted near the shaded area, suggesting that complex exsolution textures involving Ilmss, Mtss and Hemss form upon cooling

significantly lower than for pure stoichiometric ilmenite which contains 52.75 wt.% TiO₂ (Deer, 1985), and 37.21–57.54 wt.% (45.21 wt.% in average) FeO(T). A higher content of TiO₂ than the stoichiometric value occurs when Ti is leached with other cations during low-temperature diagenesis; conversely, a lower TiO₂ content indicates the existence of hematite and/or magnetite that is exsolved with ilmenite (Rao *et al.* 2014). The latter phenomenon is predominantly witnessed in petrographic studies with magnetite lamellae (Fig. 5), containing up to 78.91–98.25 wt.% (96.13 wt.% in average) FeO(T) and 0.00–0.63 wt.% (0.24 wt.% in average) TiO₂ measured.

Ilmenite or Fe-Ti oxides are widespread accessory minerals in igneous and metamorphic rocks. In the series of solid solutions in the ternary phase diagram of FeO–Fe₂O₃–TiO₂ (Fig. 6a), the end members are ferropseudobrookite (fsp-Fe-Ti₂O₅)-pseudobrookite (psb-Fe₂TiO₅), ilmenite-hematite and ulvöspinel (Fe₂TiO₄)-magnetite. The fsp-psb series applies only to high Ti and high temperature conditions ($T > 800^{\circ}\text{C}$), and is not discussed further (i.e. at lower temperatures both fsp and psb become unstable compared to ilmenite, rutile and hematite). In contrast, there is complete miscibility (solid solution) between ilmenite and hematite at temperatures $> 800^{\circ}\text{C}$. However, during crystallization and cooling, hematite and ilmenite segregate to form titanohematite, which is characterized by lamellae of hematite in varying amounts in which ilmenite is intercalated. Titanomagnetite can also develop in the FeO–Fe₂O₃–TiO₂ system. The two spinels magnetite and ulvöspinel are completely miscible at high temperatures ($T > 600^{\circ}\text{C}$). As the temperature drops, the rate of segregation into magnetite, ilmenite and ulvöspinel depends on the prevailing oxygen partial pressure and also the Fe:Ti ratio. Yet a complete segregation into pure magnetite and ulvöspinel does not take place in nature. Ilmenite, in addition, can be exsolved in the octahedral magnetite in the form of fine lamellae, although it depends on the cooling rate, since the slower the cooling, the coarser the segregation structure is. Due to the preferred incorporation of Fe instead of Ti, the content of TiO₂ in ilmenite can be lower compared to the stoichiometric value reported in the literature (52.65 wt.%) (Rahman *et al.* 2020), which is consistent with our studied ilmenites (Fig. 6a).

Ilmenite grains were only found in borehole GDH-73, where a common intergrowth pattern was found in ilmenites coexisting with magnetite. The concentration of MnO indicates the ilmenite source is of intrusive igneous origin i.e., gabbroic and granodioritic protoliths (Fig. 6b). Based on the ILMAT method for calculating the crystallization

temperature and oxygen fugacity of the ilmenite-magnetite pairs, the calculated temperatures (T) and oxygen fugacities for the coexisting magnetite and ilmenite assemblages indicate a large range of variation in T range from 522°C to 809°C with oxygen fugacities (f_{O_2}) of $10^{-23.9}$ to $10^{-11.9}$ (Supp. Table I). Plotting the temperature and oxygen fugacity ranges in Fig. 6c indicates that the Fe-Ti oxide mineral assemblages were equilibrated in a T- f_{O_2} field that is very close to the Ni/NiO buffer curve, signifying a crustal source (Buddington *et al.* 1964). The composition of ilmenites originating from tholeiitic magmas typically have MgO contents <3 wt.% and are usually a late crystallizing mineral (Haggerty 1976; Reynolds 1983), whereas ilmenites with high MgO contents (4 to 10 wt.%) are typically formed in basaltic magma at the early stage of crystallization (Cawthorn *et al.* 1985). The ilmenites in GDH-73 have MgO contents varying between 0.00–4.79 wt.% MgO indicating that the parent rocks were mostly tholeiitic magmas. It is likely however that the studied ilmenites were deposited in Hakimpur basin from different sources. In general, ilmenite forms from acidic igneous rocks in a late phase of crystallization, which is accompanied by a significant replacement of Fe by Mn and a minor replacement by Mg, which usually accounts for >1 wt.% MgO (Haggerty, 1976; Reynolds *et al.* 1983; Cawthorn *et al.* 1985; Lipman *et al.* 1971).

Mineral chemistry of zircon

The compositions of the zircon grains have ZrO₂ contents in the range between 53.58 and 63.47 wt.% and SiO₂ contents between 17.50 and 19.80 wt.% (Table 3). Minor amounts of other elements are also present in the zircons and these include 1.55–13.01 wt.% FeO, 8.06–16.14 wt.% of HfO₂ and 0.05–1.03 wt.% of TiO₂ (Table 3). The content of HfO₂ in the zircons is characteristic of zircons formed in granitic pegmatites. The most Hf-enriched zircons occur in intrusive rocks in which the abundance of Hf in zircon increases with magmatic differentiation (Sawka *et al.* 1988; Wark *et al.* 1993; Hoskin *et al.* 2000). According to Linnen and Keppler (2002), the Zr and Hf fractionation in zircon-crystallizing melts (i.e. metaluminous and peraluminous granitic melts) will decrease the Zr/Hf ratio of the residual melt, whereas it causes the enrichment of HfO₂ in zircon. The composition of metamorphic zircon in equilibrium with an anatectic melt is not significantly different from that of igneous zircon (Rubatto *et al.* 2002). The only obvious systematic difference between igneous zircon and metamorphic zircon is the Th/U ratio, which is very low for the latter (<0.07) (Rubatto *et al.* 2002). Unfortunately, the value of U was not measured in this study.

In order to calculate zircon saturation temperature, the model proposed by Boehnke *et al.* (2013) was used, which is as follows:

$$T (K) = \frac{(10108 \pm 32)}{\ln DZr + (1.16 \pm 0.15)(M - 1) - (1.48 \pm 0.09)}$$

$$\text{Where, } \ln DZr = \frac{Zr (ppm) \text{ in zircon}}{Zr (ppm) \text{ in melt}}, \text{ and } M = \frac{Na+K+2Ca}{Al Si}$$

In particular, the calculation of M is required to convert wt.% oxides to atomic fractions, renormalize to total moles, and then insert the molar fractions of Na, K, Ca, Al, and Si (over the total number of moles) into the M formulation. Using the thermometer, the calculated temperature of the studied zircon ranges from 677 to 692°C.

Mineral chemistry of monazite

Monazite and xenotime, orthophosphate minerals are included in the idealized formula of A(PO₄) and REE(PO₄) respectively, where ions of REE belonged to A-site can be substituted by non-REE species by the following: $2REE^{3+} \leftrightarrow Ca^{2+} + Th^{4+}$, which is similar to the substitution occurred in cheralite [Ca,Th(PO₄)₂] (Williams *et al.* 2007). In monazite, a coupled substitution is required in a second series of compositional exchange that occurs at the A-site and tetrahedral site simultaneously: $P^{5+} + REE^{3+} \leftrightarrow Si^{4+} + Th^{4+}$. Huttonite [Th(SiO₄)], a rare monoclinic mineral, is generated in high-temperature magmatic as well as metamorphic rocks (i.e. granulite facies) (Kucha 1980). Thus, monazite [2REE(PO₄)], cheralite [Ca,Th(PO₄)₂] and huttonite [2Th(SiO₄)] form the three end members of a ternary system (Wu *et al.* 2019). The average end-member compositions of the studied monazites comprise of 87.39 % monazite, 7.18 % huttonite and 5.44 % cheralite (Table IV), which are classified as monazite (Pyle *et al.* 2001).

Twenty-two points were analyzed on monazite grains to determine if there was any age difference between the core and rim, if any. However, in all cases, the core and rim of monazite grains indicated almost uniform ages. The ThO₂ concentrations of the analyzed monazite grains range from 3.83 to 6.12 wt.%, while UO₂ concentrations vary from 0.16 to 0.35 wt.%, and those of PbO lie between 0.35 and 0.53 wt.% (Table IV). Despite these variations, single grain core to rim shows largely uniform PbO/ThO₂ ratios (0.08–0.10), suggesting monazite formation occurred in a single thermal event. The age was obtained from 22 concordant analyses, yielding a weighted mean age of 1728 ± 28 Ma (MSWD = 2.3; Fig. 7a, b), which is consistent to the crystallizing age of the Palaeoproterozoic basement rocks in Bangladesh (Hossain *et al.* 2007; Ameen *et al.* 2007).

Table III. Representative SEM-EDS analysis of zircon (wt.%) sourced from Hakimpur BIF deposits (SVT-16)

wt.%	F3_2	F27_10	F30_1	F31_1	F3106	F3109	F3110	F3111	F3112	F3113
ZrO ₂	62.95	53.72	60.82	62.52	56.60	63.47	59.75	58.65	59.49	59.15
HfO ₂	9.24	14.06	13.27	13.92	11.06	8.06	16.14	11.67	12.31	14.96
SiO ₂	19.62	18.12	19.16	19.75	18.18	19.80	18.78	18.66	18.53	18.60
TiO ₂	0.10	0.65	0.25	0.72	0.05	0.84	0.53	1.03	0.28	0.89
FeO	7.34	4.35	5.46	2.92	10.02	5.48	1.55	7.94	7.25	3.33
MnO	0.27	0.00	1.02	0.00	0.67	0.00	0.00	0.00	0.00	0.00
CaO	0.00	6.92	0.00	0.14	0.00	0.51	1.00	0.86	0.77	2.72
Cr ₂ O ₃	0.09	0.85	0.01	0.03	1.10	0.00	0.86	0.30	0.03	0.00
ThO ₂	0.00	0.76	0.00	0.00	1.66	0.64	1.33	0.00	0.00	0.00
	99.61	99.44	99.98	100.00	99.33	98.79	99.95	99.11	98.66	99.65
Based on 4 oxygen										
Zr	1.09	0.95	1.07	1.09	1.01	1.10	1.06	1.03	1.06	1.04
Hf	0.09	0.15	0.14	0.14	0.12	0.08	0.17	0.12	0.13	0.15
Th	0.00	0.01	0.00	0.00	0.01	0.01	0.01	0.00	0.00	0.00
Ca	0.00	0.27	0.00	0.01	0.00	0.02	0.04	0.03	0.03	0.11
Ti	0.00	0.02	0.01	0.02	0.00	0.02	0.01	0.03	0.01	0.02
Fe	0.22	0.13	0.16	0.09	0.31	0.16	0.05	0.24	0.22	0.10
Cr	0.00	0.02	0.00	0.00	0.03	0.00	0.02	0.01	0.00	0.00
Mn	0.01	0.00	0.03	0.00	0.02	0.00	0.00	0.00	0.00	0.00
ΣZr site	1.42	1.55	1.41	1.34	1.50	1.39	1.37	1.46	1.45	1.43
Si	0.70	0.66	0.69	0.70	0.67	0.70	0.68	0.67	0.68	0.67
ΣSi site	0.70	0.66	0.69	0.70	0.67	0.70	0.68	0.67	0.68	0.67
T (°C)	678	692	681	678	687	677	682	684	683	683

Table III. Continue

wt.%	F3114	F3115	F3116	F3117	F3118	F3119	Avg.	Min	Max
ZrO ₂	53.58	58.27	61.47	60.48	58.33	58.46	59.23	53.58	63.47
HfO ₂	12.74	13.90	12.57	13.89	16.03	13.54	12.96	8.06	16.14
SiO ₂	17.50	18.58	19.02	19.77	19.71	19.30	18.94	17.50	19.80
TiO ₂	0.44	0.46	0.63	0.21	0.80	0.59	0.53	0.05	1.03
FeO	13.01	8.22	4.07	2.33	1.69	2.08	5.44	1.55	13.01
MnO	0.27	0.00	0.00	0.00	0.00	0.56	0.17	0.00	1.02
CaO	0.00	0.00	1.58	1.36	3.27	4.17	1.46	0.00	6.92
Cr ₂ O ₃	0.50	0.00	0.00	0.22	0.00	0.00	0.25	0.00	1.10
ThO ₂	0.00	0.00	0.00	0.94	0.00	0.37	0.36	0.00	1.66
	98.04	99.44	99.33	99.20	99.83	99.07	99.34	98.04	100.00
Based on 4 oxygen									
Zr	0.98	1.04	1.08	1.06	1.02	1.03	1.04	0.95	1.10
Hf	0.14	0.14	0.13	0.14	0.16	0.14	0.13	0.08	0.17
Th	0.00	0.00	0.00	0.01	0.00	0.00	0.00	0.00	0.01
Ca	0.00	0.00	0.06	0.05	0.13	0.16	0.06	0.00	0.27
Ti	0.01	0.01	0.02	0.01	0.02	0.02	0.01	0.00	0.03
Fe	0.41	0.25	0.12	0.07	0.05	0.06	0.17	0.05	0.41
Cr	0.01	0.00	0.00	0.01	0.00	0.00	0.01	0.00	0.03
Mn	0.01	0.00	0.00	0.00	0.00	0.02	0.01	0.00	0.03
ΣZr site	1.56	1.45	1.41	1.35	1.38	1.43	1.43	1.34	1.56
Si	0.66	0.68	0.68	0.71	0.71	0.70	0.69	0.66	0.71
ΣSi site	0.66	0.68	0.68	0.71	0.71	0.70	0.69	0.66	0.71
T (°C)	692	685	680	681	684	684	683	677	692

Note: Temperature is measured following the thermometer of Boehnke *et al.* (2013)

Magmatic monazite, along with other early accessory minerals such as zircon and xenotime, generally occurs as an interstitial mineral in rock-forming minerals such as quartz, feldspars and biotite, while hydrothermal monazite typically occurs as inclusions in secondary phyllosilicates, quartz, albite and amphiboles, or grain boundaries with sulfides and oxides (Schandl *et al.* 2004). The igneous and metamorphic monazite differs from the hydrothermal monazite mainly in the higher ThO₂ content and Th/Ce ratio (>1 wt.% and >0.04 respectively) (Fig. 8a). The monazite samples from the bore hole GDH-68

(SXE-3) have high ThO₂ contents (avg. 4.73 wt.%), suggesting an igneous and metamorphic origin (Fig. 8a). Acting upon the compositional difference of igneous, metamorphic, hydrothermal, and carbonatite monazite, Wu *et al.* (2019) proposed a geochemical discrimination diagram to understand the rock type in which it occupies. Accordingly, almost all monazite samples in this study were classified as metamorphic (Fig. 8b). This is further supported by its coexistence with biotite, disseminated in the biotite-schist rocks (Fig. 7a).

Table IV. Representative electron probe micro analysis of monazite (wt.%) sourced from Hakimpur BIF deposits in Bangladesh

No.	1	2	3	4	5	6	7	8	9	10	11	12	13	14
SiO ₂	0.48	0.51	0.30	0.47	0.53	0.50	0.48	0.55	0.62	0.41	0.31	0.63	1.36	0.52
UO ₂	0.30	0.23	0.30	0.30	0.31	0.23	0.16	0.21	0.26	0.27	0.35	0.33	0.32	0.29
ThO ₂	4.20	5.30	4.24	4.38	4.16	5.23	5.97	4.72	4.09	4.51	4.16	4.23	3.98	4.67
PbO	0.40	0.46	0.42	0.41	0.38	0.47	0.52	0.40	0.35	0.43	0.42	0.40	0.37	0.42
Ce ₂ O ₃	27.29	26.04	27.57	27.81	27.99	27.01	25.74	27.03	27.59	27.61	27.92	27.93	27.75	27.51
La ₂ O ₃	14.00	13.21	13.51	13.96	14.17	13.13	12.19	13.18	13.39	13.21	13.64	13.84	14.00	14.07
Sm ₂ O ₃	2.16	2.05	2.15	2.10	2.08	1.99	2.02	2.24	2.16	2.19	2.10	2.14	2.09	2.09
Nd ₂ O ₃	12.01	11.50	11.76	11.69	12.10	11.48	10.97	11.79	12.16	11.71	11.88	12.26	11.92	12.00
Pr ₂ O ₃	4.00	3.84	3.93	3.99	4.06	3.85	3.74	3.98	4.07	4.04	4.12	4.12	3.96	4.01
CaO	0.94	1.43	1.19	1.04	0.93	1.40	1.72	1.14	0.87	1.17	1.16	0.93	0.81	1.15
Y ₂ O ₃	2.21	2.73	2.31	2.31	2.28	2.73	2.88	2.30	2.07	2.30	2.23	2.18	2.08	2.32
P ₂ O ₅	28.41	28.28	27.09	27.45	27.38	27.30	27.17	27.14	27.10	27.36	27.90	28.85	28.66	29.17
Total	96.40	95.59	94.76	95.91	96.36	95.32	93.54	94.67	94.73	95.21	96.20	97.85	97.29	98.19
Based on 4 oxygen														
Si	0.02	0.02	0.01	0.02	0.02	0.02	0.02	0.02	0.03	0.02	0.01	0.02	0.05	0.02
P	0.98	0.98	0.96	0.96	0.96	0.96	0.96	0.96	0.96	0.96	0.97	0.98	0.97	0.98
ΣP	1	1	1	1	1	1	1	1	1	1	1	1	1	1
U	0.00	0.00	0.00	0.00	0.00	0.00	0.00	0.00	0.00	0.00	0.00	0.00	0.00	0.00
Th	0.04	0.05	0.04	0.04	0.04	0.05	0.06	0.04	0.04	0.04	0.04	0.04	0.04	0.04
Pb	0.00	0.00	0.00	0.00	0.00	0.00	0.00	0.00	0.00	0.00	0.00	0.00	0.00	0.00
Ce	0.41	0.39	0.42	0.42	0.42	0.41	0.40	0.41	0.42	0.42	0.42	0.41	0.40	0.40
La	0.21	0.20	0.21	0.21	0.22	0.20	0.19	0.20	0.21	0.20	0.21	0.20	0.21	0.21
Sm	0.03	0.03	0.03	0.03	0.03	0.03	0.03	0.03	0.03	0.03	0.03	0.03	0.03	0.03
Nd	0.17	0.17	0.18	0.17	0.18	0.17	0.16	0.18	0.18	0.17	0.17	0.17	0.17	0.17
Pr	0.06	0.06	0.06	0.06	0.06	0.06	0.06	0.06	0.06	0.06	0.06	0.06	0.06	0.06
Ca	0.04	0.06	0.05	0.05	0.04	0.06	0.08	0.05	0.04	0.05	0.05	0.04	0.03	0.05
Y	0.05	0.06	0.05	0.05	0.05	0.06	0.06	0.05	0.05	0.05	0.05	0.05	0.04	0.05
ΣA	1	1	1	1	1	1	1	1	1	1	1	1	1	1
End member														
Monazite	0.93	0.90	0.95	0.95	0.96	0.93	0.90	0.94	0.95	0.94	0.94	0.92	0.91	0.91
Cheralite	0.05	0.07	0.06	0.05	0.05	0.07	0.08	0.06	0.04	0.06	0.06	0.05	0.04	0.05
Huttonite	0.06	0.07	0.05	0.06	0.06	0.07	0.08	0.07	0.06	0.06	0.05	0.06	0.09	0.06
	1.031	1.036	1.063	1.059	1.064	1.065	1.057	1.059	1.058	1.057	1.049	1.031	1.038	1.027

Table IV. Continue

No.	15	16	17	18	19	20	21	22
SiO ₂	0.51	0.55	0.55	0.61	0.61	0.80	1.10	5.34
UO ₂	0.20	0.29	0.27	0.16	0.17	0.20	0.25	0.28
ThO ₂	4.98	4.71	4.87	6.08	6.12	5.10	4.45	3.83
PbO	0.46	0.45	0.46	0.53	0.52	0.44	0.39	0.37
Ce ₂ O ₃	26.84	27.57	27.34	26.28	26.33	26.60	27.38	26.48
La ₂ O ₃	13.16	13.97	13.45	12.91	12.68	13.17	13.50	12.90
Sm ₂ O ₃	2.03	2.26	2.11	2.16	2.08	2.16	2.24	2.07
Nd ₂ O ₃	11.49	12.12	12.13	11.54	11.71	12.15	12.67	11.96
Pr ₂ O ₃	3.92	3.93	3.91	3.93	3.68	4.05	4.01	3.83
CaO	1.54	1.17	1.20	1.68	1.68	1.30	1.02	0.98
Y ₂ O ₃	2.66	2.32	2.62	2.82	2.86	2.49	2.21	2.03
P ₂ O ₅	28.86	28.89	28.90	29.60	29.34	29.34	28.88	27.67
Total	96.64	98.21	97.82	98.29	97.77	97.81	98.11	97.74
Based on 4 oxygen								
Si	0.02	0.02	0.02	0.02	0.02	0.03	0.04	0.20
P	0.98	0.97	0.98	0.98	0.98	0.98	0.97	0.89
ΣP	1	1	1	1	1	1	1	1
U	0.00	0.00	0.00	0.00	0.00	0.00	0.00	0.00
Th	0.05	0.04	0.04	0.05	0.06	0.05	0.04	0.03
Pb	0.00	0.00	0.00	0.00	0.00	0.00	0.00	0.00
Ce	0.39	0.40	0.40	0.38	0.38	0.38	0.40	0.37
La	0.19	0.21	0.20	0.19	0.18	0.19	0.20	0.18
Sm	0.03	0.03	0.03	0.03	0.03	0.03	0.03	0.03
Nd	0.16	0.17	0.17	0.16	0.17	0.17	0.18	0.16
Pr	0.06	0.06	0.06	0.06	0.05	0.06	0.06	0.05
Ca	0.07	0.05	0.05	0.07	0.07	0.06	0.04	0.04
Y	0.06	0.05	0.06	0.06	0.06	0.05	0.05	0.04
ΣA	1	1	1	1	1	1	1	1
End member								
Monazite	0.90	0.92	0.91	0.87	0.87	0.89	0.91	0.83
Cheralite	0.07	0.06	0.06	0.07	0.08	0.06	0.05	0.04
Huttonite	0.07	0.06	0.07	0.08	0.08	0.08	0.08	0.24
	1.032	1.036	1.034	1.024	1.027	1.024	1.039	1.114

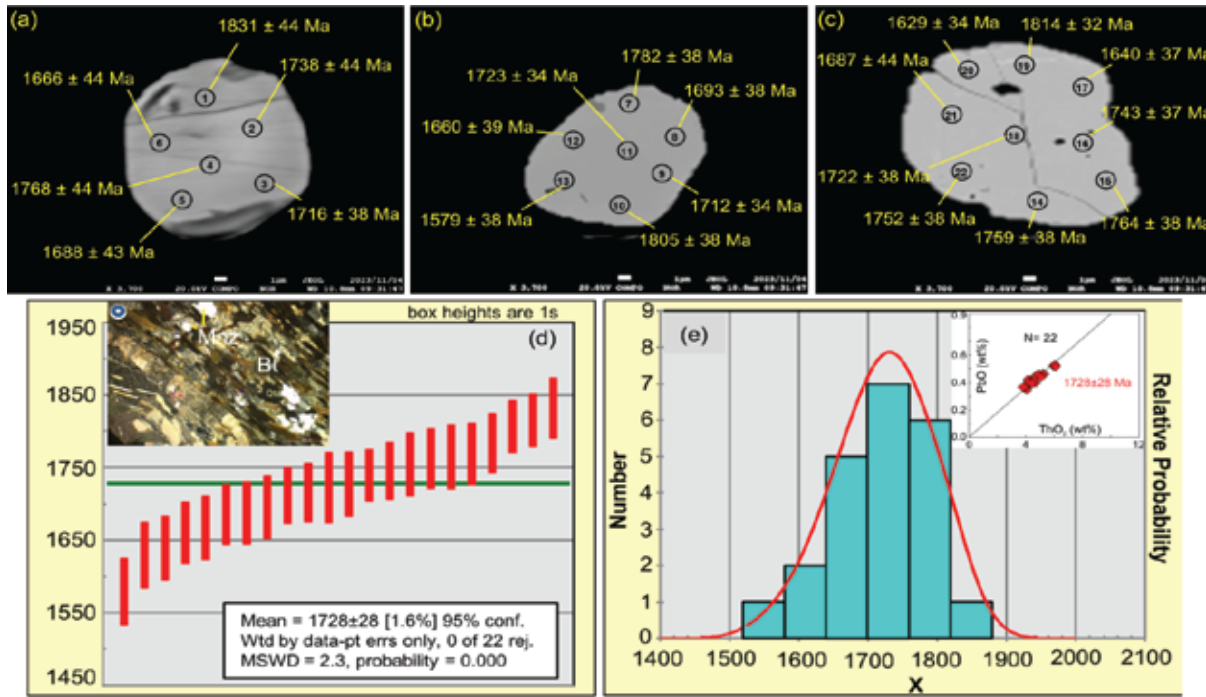


Fig. 7. (a) Representative Th-U-Pb weighted average age plots of monazites. The inset shows part of a thin section of a biotite-schist (sample SXE-3), where monazites were mostly coexisting with biotite. (b) A bar diagram with an associated fitting curve for the Hakimpur BIF deposits in Bangladesh. Mnz- monazite, and Bt- biotite

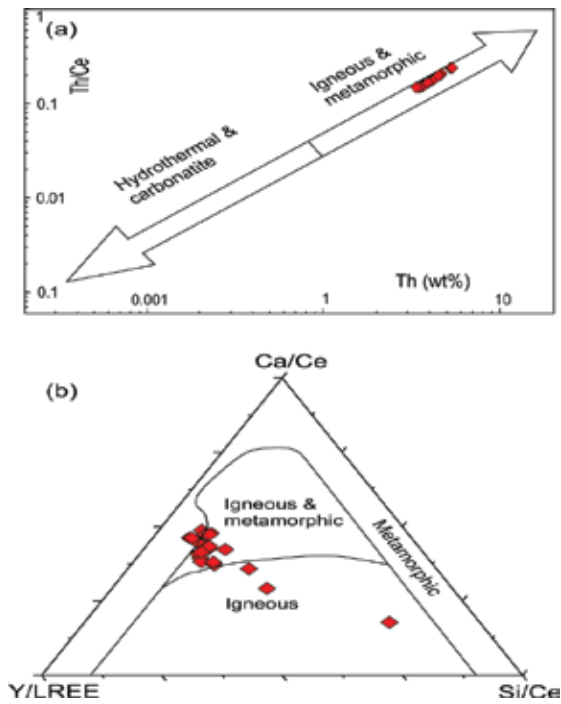


Fig. 8. (a) and (b) the discrimination diagram for defining monazite origin (Pyle *et al.* 2001)

Discussion

Detrital input in BIF and BIF hosted rocks

In most cases, iron formations are free of detritus (Bau *et al.* 1996; Beukes *et al.* 1990; Dymek *et al.* 1988; Peng *et al.* 2018), nevertheless, terrigenous contamination is not uncommon worldwide (Aoki *et al.* 2018; Ghosh *et al.* 2017; Gourcerol *et al.* 2016; Hou *et al.* 2019; Pecoits *et al.* 2009; Sun *et al.* 2018; Sylvestre *et al.* 2017; Tamehe *et al.* 2018). Even, chemically precipitated pure BIFs may co-exist with impure BIFs within the same depositional environment (Haugaard *et al.* 2013; Viehmann *et al.* 2015; Wang *et al.* 2015; Barrote *et al.* 2017; Ndime *et al.* 2019).

As observed from the petrographic study, all rock types in the Hakimpur iron deposits were subjected to moderate to high-grade metamorphic alteration with varying degrees of migmatization. Analysis of the chemistry of the rocks of the Hakimpur region may be used to provide constraints on the petrogenesis and tectonic setting (Liu *et al.* 2012; Zhang *et al.* 2012). Overall, the oxides particularly Al_2O_3 , MgO and TiO_2 , are excellent monitors for detecting terrigenous contamination (Manikyamba *et al.* 1993; Arora *et al.* 1995; Rao *et al.* 1995). To understand the nature of their protoliths, we used an Al_2O_3 vs (Na_2O+K_2O) discrimination diagram with the results showing that all samples plot in the field

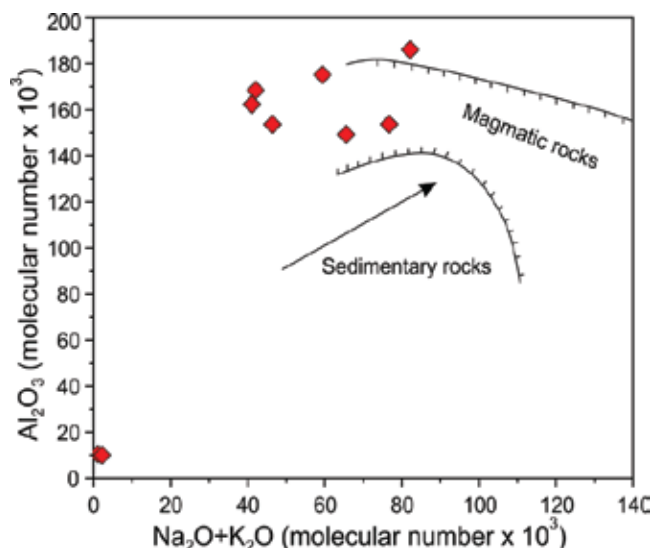


Fig. 9. Al_2O_3 – $(\text{Na}_2\text{O}+\text{K}_2\text{O})$ diagrams for differentiating sedimentary from igneous rocks (Defant *et al.* 2002). The BIF samples cluster in the sedimentary rocks field whereas the host rocks plot in the magmatic area. Noteworthy, the arrowhead represents the direction of a lower concentration of sub-greywacke and feldspar sandstone. The molecular number is calculated by coordinates multiplied by 1000

of magmatic rocks except the BIF samples (e.g. SXE-1 and SVT-15) (Fig. 9). On the SiO_2 – $(\text{Na}_2\text{O}+\text{K}_2\text{O})$ diagram (Defant *et al.* 2002), the protolith of the amphibolite and biotite-schist are more likely gabbroic rock type, albeit quartzite shows ijolitic nature (Fig. not shown), which are very misleading because enrichment of Fe is indicating basic and ultrabasic in the TAS diagram. However, this phenomenon is common in the case of the BIF. Hence, compositionally the amphibolite and biotite-schist samples manifest basic, whereas BIFs indicate ultrabasic, with mean SiO_2 contents of 45.24 wt.% and 22.18 wt.% respectively. Surprisingly, compared to the typical composition of basic and ultrabasic rocks (Winter, 2001), the content of Al_2O_3 , MgO and TiO_2 in BIF, amphibolite and biotite-schist resemble ambiguous (Table II), indicating the protoliths are sedimentary. The petrographic studies of these rocks support this view too, because the sources of sedimentary signatures are obvious in the samples particularly (i) quartz overgrowth and preferred orientation of banding and lamination in BIFs (Fig. 3e, g, m and a–f, respectively), (ii) chertification in biotite schist (Fig. 3g), (iii) metamict and eroded zircon in amphibolite, and (iv) granoblastic polygonal quartz in quartzite (Fig. 3k).

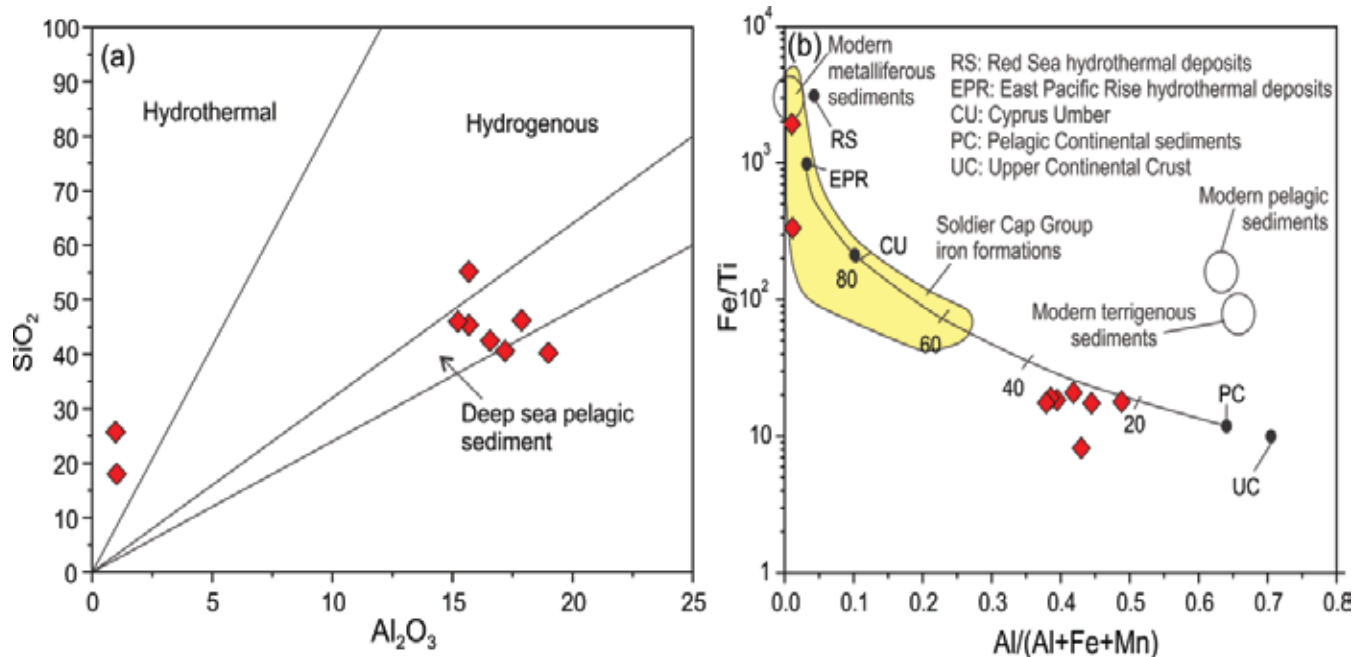


Fig. 10. SiO_2 vs. Al_2O_3 discrimination diagram indicating the hydrothermal affinity of the studied BIF. (b) Composition of the Hakimpur BIF and its host rocks plotted on a Fe/Ti vs. $\text{Al}/(\text{Al}+\text{Fe}+\text{Mn})$ discrimination diagram (Teutsong *et al.* 2017). This diagram is proposed for estimating the relative contribution from hydrothermal inputs in the fluid from which BIF precipitated

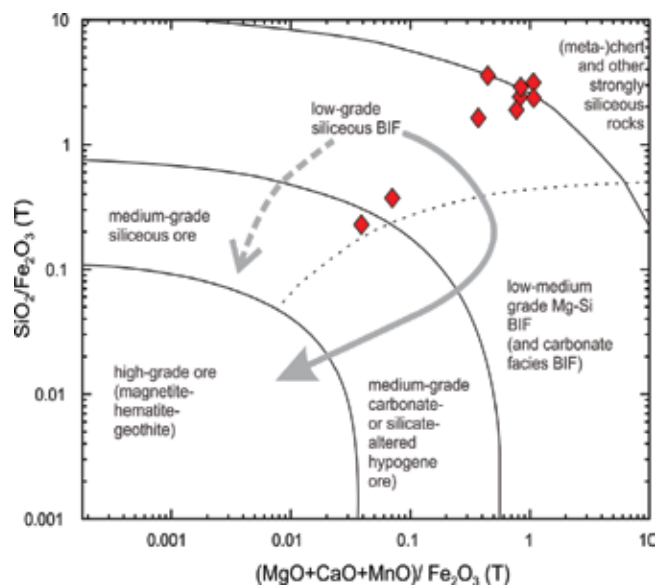


Fig. 11. The discrimination diagram for BIF, altered BIF, medium- and high-grade ore implementing whole-rock geochemistry of major oxide ratios $(\text{MgO} + \text{CaO} + \text{MnO})/\text{Fe}_2\text{O}_3(\text{T})$ versus $\text{SiO}_2/\text{Fe}_2\text{O}_3(\text{T})$ (Hagemann *et al.* 2016). Arrows showing alteration trends from MgO + CaO + MnO-rich to -poor stages in the discrimination fields

The studied BIFs are chemically pure that constitute the major components of SiO_2 and $\text{Fe}_2\text{O}_3(\text{T})$ (Table II), and they retain with low concentrations of Al_2O_3 and TiO_2 ($\text{Al}_2\text{O}_3 + \text{TiO}_2 = 1.12\text{--}1.26$ wt.%). Because Al_2O_3 and TiO_2 cannot be introduced in solution, they are commonly defined as traces of detrital contamination in BIFs (Basta *et al.* 2011; Lan *et al.* 2014), which indicates that terrigenous clastic materials were involved during the deposition of the Hakimpur BIF. Additionally, all the major elements (Fe_2O_3 , Al_2O_3 , TiO_2 , MnO, MgO, CaO and Na_2O , except K_2O) of biotite schist, quartzite and amphibolite show weak to strong negative correlation with SiO_2 (Fig. 4), which may imply incorporation of terrigenous components.

Source of the hakimpur BIF

Banded iron formations are chemically precipitated sediments formed from iron and silica solutions consisting of a mixture of seawater and hydrothermal fluids. The main contaminants are usually terrigenous sediments carried by rivers or winds, deposited by volcanic activity (Kato *et al.* 1998; Klein *et al.* 1989) or pelagic sediments (Lascelles *et al.* 2007). The technique for distinguishing the sources of seawater, hydrothermal, biogenic and detrital is defined particularly based on the mineralogical, chemical and isotopic evidence.

Based on the relative abundance of SiO_2 and Al_2O_3 (Fig. 10a), Bonatti (1975) proposed that hydrothermal metal-rich deposits can be distinguished from hydrogenous deposits that occurred by diagenetic processes. In this diagram, BIFs (SXE-3 and SVT-15) from the studied samples plot in the hydrothermal field, whereas the majority of the samples cluster in the field of deep-sea pelagic sediment. The Fe/Ti vs. $\text{Al}/(\text{Al} + \text{Fe} + \text{Mn})$ diagram also shows consistent results (Fig. 10b; Teutsong *et al.* 2017). In the diagram, pure hydrothermal chemical sediments are enriched in Fe and Mn, whereas Al and Ti characterize the clastic or volcanic material (González *et al.* 2009). This diagram illustrates that the studied BIFs cluster close to the hydrothermal deposits, whereas the BIF-hosted rocks plot closer to pelagic continental sediments (Fig. 10b). Partly due to scavenging processes, the chemical composition of iron-rich hydrothermal precipitates is very similar to the hydrogenous precipitates (Marchig *et al.* 1982). Therefore, all of the methods proposed by Bischoff and Rosenbauer (1977); Boström (1975) and Dymond *et al.* (1976) should be used carefully. It is evident from Fig. 10b, where, the modern metalliferous sediments cluster near to hydrothermal deposits, and cannot distinguish between hydrothermal and diagenetic metalliferous sediments. Mineralogical and paleontological investigations offer the possibility of differentiating between them (Marchig *et al.* 1982). They documented fossil or trace of fossil boundary is typically present in the fraction of diagenetic metalliferous sediments, in contrast, well-crystallized goethite exists in hydrothermal metalliferous sediments. The studied samples are diagenetic metalliferous sediments, since the former evidence is well-preserved in the sample SXE-14 (Fig. 3f), in which the fossil contents were disappeared yet to be diminished its boundary during metamorphism.

Based on the ratios of $\text{SiO}_2/\text{Fe}_2\text{O}_3(\text{T})$ and $(\text{MgO} + \text{CaO} + \text{MnO})/\text{Fe}_2\text{O}_3(\text{T})$ (Fig. 11) (Hagemann *et al.* 2016; Angerer *et al.* 2012), the studied BIFs show low- to medium-grade siliceous BIF, where Fe-rich mafic mineral i.e. amphibole and biotite is very less. Compared to this, the associated host rocks i.e. biotite schist, quartzite and amphibolite contain high amount of amphibole and biotite. Petrographic study and geochemical classification reveal that the precursor mineral might be clay minerals, which was changed into the following minerals subsequently at a certain pressure and temperature during metamorphism:

Clay (illite) \rightarrow chlorite \rightarrow biotite \rightarrow amphibole.

In our studies, magnetite is the dominant Fe-rich mineral of the BIF. Due to the high degree metamorphism and recrystallized habit of the magnetite crystals, it is not possible to accurately link the evolution of this mineral to the primary

process of iron precipitation from seawater. As suggested in many models of BIF formation, the primary iron mineral precipitated directly from seawater was most likely an Fe^{3+} oxyhydroxide, a mixed valence Fe-silicate or a Fe^{2+} -carbonate (e.g., siderite) (Fischer *et al.* 2009). Studies of low-grade metamorphosed BIF suggest that such primary minerals often transform into Fe-rich minerals (e.g., magnetite, hematite and siderite) and several iron silicate phases through a variety of possible abiotic or microbial-mediated processes (Bontognali *et al.* 2013; Smith *et al.* 2013; Posth *et al.* 2013). In BIF, siderite is transformed into magnetite by diagenetic processes.

Implication for the age of the basement complex and correlation with the BIF

Recent geochronological studies of basement rocks in the northwestern part of Bangladesh indicate that Paleoproterozoic (1720–1730 Ma) tonalitic/granitic pegmatite to diorite rocks are considered a continuation of the Central Indian Tectonic Zone (CITZ) in the Columbia supercontinent configuration (Hossain *et al.* 2007; Ameen *et al.* 2007) that occur in the Maddhapara area at shallow depths (128 m). The overlying stratigraphic column is covered by successive units of the Permian Gondwana Group, the Pliocene Dupi Tila formation, the Pleistocene Barind Clay formation and Recent alluvium (Hossain *et al.* 2009). The age of the Palaeoproterozoic basement rocks in Bangladesh is similar to the age of metamorphic event in the Hakimpur BIF deposits (Fig. 7a). In Table IV, monazites show uniform PbO/ThO_2 ratios giving an age of 1728 Ma (mean), suggesting the protolith was subjected to a single metamorphic event. In order to estimate the same age of the basement rock and the Hakimpur BIF deposits, it can be inferred that the metamorphic alteration in the BIF's mineral assemblages was influenced by the tectonomagmatic nature of the crystalline basement magma.

The calculated temperature (T) conditions of the zircon and the coexisting magnetite and ilmenite assemblages are 677–692°C and 522–809°C (at $10^{-23.9}$ to $10^{-11.9}$ f_{O_2}), respectively (Table III and), which is consistent with the P-T conditions (680–725°C at 4.9–6.4 kbar) that occurred during crystallization of dioritic basement rock in Bangladesh (Hossain *et al.* 2009). Based on the T- f_{O_2} conditions (Fig. 6c), the Fe-Ti oxide minerals hosted in felsic rocks are sourced from crustal origin of tholeiitic magma. Also, the content of Hf indicates that zircons were sourced from felsic suits. The studied BIF and BIF-hosted rocks are seemingly formed from a mafic and/or ultramafic protolith, however additional evidence such as the presence of olivine and pyroxene was not present in the petrographic studies. Since the studied BIF and BIF-hosted rocks are developed in sedimentary protolith,

the lack of mafic and ultramafic components (with lower Mg content; Table II) in our studies may indicate felsic nature, which is not uncommon in BIF deposits throughout the world (Hagemann *et al.* 2016).

Conclusions

The Hakimpur BIF deposit is a recently discovered iron deposit located in the Basement Complex in Bangladesh. The iron deposit is characterized by the presence of BIF, biotite schist, quartzite and amphibolite. Combining whole rock geochemistry, mineral geochemistry and monazite geochronological studies of the Hakimpur BIFs, the following conclusions were made:

Variable high $\text{Fe}_2\text{O}_3+\text{SiO}_2$ contents and the texture in petrographic studies suggest that their chemical precipitation was influenced by variable terrigenous input, and later metamorphosed by hydrothermal influence or orogenic activity due to magmatism of Palaeoproterozoic basement rock in surrounding areas.

Monazite geochronology reveals that the Hakimpur BIFs experienced a single metamorphic event that occurred at ca. 1728±28 Ma during the Basement rock's magmatic event activated.

Thermometry of the studied minerals (zircon, and coexisting magnetite and ilmenite assemblages) demonstrate the studied rocks went through medium grade metamorphism, since zircon shows temperatures of 677–692°C, and the later magnetite/ilmenite assemblage display 522–809°C, which is partly consistent to crystalline temperature of the Basement rock in Bangladesh.

Author contributions

Conceptualization, A.S.M. Mehedi Hasan; Data curation, A.S.M. Mehedi Hasan, Toshiaki Tsunogae, Md. Sha Alam; Formal analysis, A.S.M. Mehedi Hasan; Funding acquisition, Methodology, A.S.M. Mehedi Hasan; Resources, Md. Ali Akbar; Supervision, Ismail Hossain and Mohammad Nazim Zaman; Visualization, Md. Sahiduzzaman and Zareen Yeasmin; Writing – original draft, A.S.M. Mehedi Hasan; Writing – review & editing.

Funding

The Director General of BPI is thanked for providing financial support for A.S.M. Mehedi Hasan for funding the project.

Acknowledgments

The authors acknowledge the financial support provided by the Bangladesh Petroleum Institute (BPI). We would like to thank the Chairman of BCSIR for supporting the laboratory's equipment at the IMMM, Joypurhat, Bangladesh. The authors are also extremely grateful to the Director General of Geological Survey of Bangladesh for providing core samples and previous reports in this research.

Conflicts of interest

The authors declare no conflict of interest.

References

- Aftabuzzaman M, Kabir S, Islam MK and Alam MS (2013), Clay mineralogy of the Pleistocene soil horizon in Barind Tract, Bangladesh, *Journal of the Geological Society of India*. **81**: 677-84. doi:10.1007/s12594-013-0089-4.
- Ameen SM, Wilde SA, Kabir MZ, Akon E, Chowdhury KR and Khan MS (2007), Paleoproterozoic granitoids in the basement of Bangladesh: A piece of the Indian shield or an exotic fragment of the Gondwana jigsaw, *Gondwana Research*. **12**(4): 380-7.
- Angerer T, Duuring P, Hagemann SG, Thorne W and McCuaig TC (2015), A mineral system approach to iron ore in Archaean and Palaeoproterozoic BIF of Western Australia, Geological Society, London, *Special Publications*. **393**(1): 81-115. doi:10.1144/SP393.11. <https://doi.org/10.1144/SP393.11>
- Angerer T, Hagemann SG and Danyushevsky LV (2012), Geochemical evolution of the banded iron formation-hosted high-grade iron ore system in the Koolyanobing Greenstone Belt, Western Australia, *Economic Geology*. **107**(4): 599-644. <https://doi.org/10.2113/econgeo.107.4.599>
- Aoki S, Kabashima C, Kato Y, Hirata T and Komiya T (2018), Influence of contamination on banded iron formations in the Isua supracrustal belt, West Greenland: Reevaluation of the Eoarchean seawater compositions, *Geoscience Frontiers*. **9**(4): 1049-1072.
- Arora M, Govil PK, Charan SN, Raj BU, Manikyamba C, Chatterjee AK and Naqvi SM (1995), Geochemistry and origin of Archean banded iron-formation from the Bababudan Schist Belt, India, *Economic Geology*. **90**(7): 2040-57.
- Baksi AK (1995), Petrogenesis and timing of volcanism in the Rajmahal flood basalt province, northeastern India, *Chemical Geology*. **121**(1-4): 73-90.
- Barrote VR, Rosiere CA, Rolim VK, Santos JO and Mcnaughton NJ (2017), The Proterozoic Guanães banded iron formations, southeastern border of the São Francisco Craton, Brazil: evidence of detrital contamination. *Geologia USP, Série Científica*. **17**(2): 303-24. DOI: <https://doi.org/10.11606/issn.2316-9095.v17-352>
- Basta FF, Maurice AE, Fontboté L and Favarger PY (2011), Petrology and geochemistry of the banded iron formation (BIF) of Wadi Karim and Um Anab, Eastern Desert, Egypt: implications for the origin of Neoproterozoic BIF, *Precambrian Research*. **187**(3-4): 277-92. doi:10.1016/j.precamres.2011.03.011.
- Bau M and Dulski P (1996), Distribution of yttrium and rare-earth elements in the Penge and Kuruman iron-formations, Transvaal Supergroup, South Africa, *Precambrian Research*. **79**(1-2): 37-55.
- Beukes NJ and Klein C (1990), Geochemistry and sedimentology of a facies transition—from microbanded to granular iron-formation—in the early Proterozoic Transvaal Supergroup, *South Africa, and Precambrian Research*. **47**(1-2): 99-139. doi:10.1016/0301-9268(90)90033-M.
- Beukes NJ and Gutzmer JE (2008), Origin and paleoenvironmental significance of major iron formations at the Archean-Paleoproterozoic boundary. doi: 10.5382/rev.15.01.
- Bhattacharya HN, Chakraborty I and Ghosh KK (2007), Geochemistry of some banded iron-formations of the Archean supracrustals, Jharkhand-Orissa region, India, *Journal of Earth System Science*. **116**: 245-59. doi:10.1007/s12040-007-0024-4.
- Bischoff JL and Rosenbauer RJ (1977), Recent metalliferous sediment in the North Pacific manganese nodule area, *Earth and planetary science letters*. **33**(3): 379-88.
- Blatt H, Tracy R and Owens B (2006), Petrology: igneous, sedimentary, and metamorphic. Macmillan. ISBN 0716737434.

- Boehnke P, Watson EB, Trail D, Harrison TM and Schmitt AK (2013), Zircon saturation re-revisited, *Chemical Geology*. **351**: 324-34.
- Boggs S (2012), Principles of Sedimentology and Stratigraphy.
- Bonatti E (1975), Metallogenesis at Oceanic Spreading Centers, *Annu. Rev. Earth Planet. Sci.* **3**: 401-431.
- Bontognali TR, Fischer WW and Föllmi KB (2013), Siliciclastic associated banded iron formation from the 3.2 Ga Moodies group, Barberton greenstone belt, South Africa, *Precambrian Research*. **226**: 116-24.
- Boström K (1975), Origin and Fate of Ferromanganous Active Ridge Sediments, Pelagic Sediments L. under Sea. 401.
- Buddington AF and Lindsley DH (1964), Iron-titanium oxide minerals and synthetic equivalents, *Journal of Petrology*. **5**(2): 310-57. doi:10.1093/petrology/5.2.310.
- Bustamante A (2005), Mössbauer spectroscopy description of limonite from Taraco, in the Huancane Province of the Puno Region, Peru. Cabrera J, Garcia V, Urday E, Abdu YA and Scorzelli RB, In ICAME 2005: Proceedings of the 28th International Conference on the Applications of the Mössbauer Effect (ICAME 2005) held in Montpellier, France, 4-9 September 2005, Volume I (Part I-II/V) 2007. Springer Berlin Heidelberg. pp. 593-597.
- Cawthorn RG, Groves DI and Marchant T (1985), Magnesian ilmenite; clue to high-Mg parental magma of the Insizwa Complex, Transkei, *The Canadian Mineralogist*. **23**(4): 609-618.
- Curry JR, Emmel FJ, Moore DG and Raitt RW (1982), Structure, tectonics, and geological history of the northeastern Indian Ocean, The ocean basins and margins: *The Indian Ocean*. 399-450.
- Dai Yanpei ZL, Changle W, Li L, Minli C, Mingtian Z and Peng X (2012), Genetic type, formation age and tectonic setting of the Waitoushan banded iron formation, Benxi, Liaoning Province, Acta Petrologica Sinica. **28**(11): 3574-3594.
- Dan W, Li XH, Guo J, Liu Y and Wang XC (2012), Paleoproterozoic evolution of the eastern Alxa Block, westernmost North China: evidence from in situ zircon U-Pb dating and Hf-O isotopes, *Gondwana Research*. **21**(4): 838-64. <https://doi.org/10.1016/j.gr.2011.09.004>
- Davis JK, Lawver LA, Norton IO and Gahagan LM (2016), New Somali Basin magnetic anomalies and a plate model for the early Indian Ocean, *Gondwana research*. **34**: 16-28. <https://doi.org/10.1016/j.gr.2016.02.010>
- Deer WA (1985), Rock-forming Minerals: Introduction to the Rock-forming Minerals, Longman.
- Defant MJ (2002), Adakites: some variations on a theme, *Acta Petrol. Sin.* **18**: 129-142.
- Duan H, Wang C, Shi K, Wang C, Chen Q, Zhu J and Qian J (2021), Insights into characterization and genesis of the Tieshanmiao banded iron formation deposit, China: Evidence from zircon U-Pb dating and geochemistry, *Ore Geology Reviews*. **138**: 104329. doi:10.1016/j.oregeorev.2021.104329.
- Dymek RF and Klein C (1988), Chemistry, petrology and origin of banded iron-formation lithologies from the 3800 Ma Isua supracrustal belt, West Greenland, *Precambrian Research*. **39**(4): 247-302.
- Dymond J, Corliss JB and Stillinger R (1976), Chemical composition and metal accumulation rates of metaliferous sediments from Sites 319, 320, and 321, Yeats, RS, Hart, SR, et al., Init. Repts. DSDP. **34**: 575-588.
- Fischer WW and Knoll AH (2009), An iron shuttle for deepwater silica in Late Archean and early Paleoproterozoic iron formation, *Geological Society of America Bulletin*. **121**(1-2): 222-35. <https://doi.org/10.1130/B26328.1>
- Geymond U, Ramanaidou E, Lévy D, Ouaya A and Moretti I (2022), Can weathering of banded iron formations generate natural hydrogen? Evidence from Australia, Brazil and South Africa, *Minerals*. **12**(2): 163.
- Ghosh R and Baidya TK (2017), Mesoarchean BIF and iron ores of the Badampahar greenstone belt, iron ore group, East Indian Shield. *Journal of Asian Earth Sciences*. **150**: 25-44.
- González PD, Sato AM, Llambías EJ and Petronilho LA (2009), Petrology and geochemistry of the banded iron formation in the Eastern Sierras Pampeanas of San Luis (Argentina): Implications for the evolution of the Nogolí Metamorphic Complex, *Journal of South American Earth Sciences*. **28**(2):89-112.

- Gourcerol B, Thurston PC, Kontak DJ, Côté-Mantha O and Biczok J (2016), Depositional setting of Algoma-type banded iron formation, *Precambrian Research*. **281**: 47-79. <https://doi.org/10.1016/j.precamres.2016.04.019>
- GSB (2020), Report on the Interpretation of Geophysical Logs of the Borehole GDH-73 at Hakimpur Upazila, Dinajpur District, Bangladesh. Unpublished Report.
- Hagemann SG, Angerer T, Duuring P, Rosière CA, Figueiredo e Silva RC, Lobato L, Hensler AS, Walde DHG (2016), BIF-Hosted Iron Mineral System: A Review. *Ore Geol. Rev.* **76**: 317–359. doi:10.1016/j.oregeorev.2015.11.004.
- Haggerty SE (1976), Opaque mineral oxides in terrestrial igneous rocks, *Oxide minerals*. 3.
- Haggerty SE (2018), Oxide Textures-a Mini-Atlas. In *Oxide minerals, De Gruyter*. 129–220. ISBN 1501508687.
- Haugaard R, Frei R, Stendal H and Konhauser K (2013), Petrology and geochemistry of the ~ 2.9 Ga Itilliarsuk banded iron formation and associated supracrustal rocks, West Greenland: Source characteristics and depositional environment, *Precambrian Research*. **229**: 150-76. <https://doi.org/10.1016/j.precamres.2012.04.013>
- Herron MM (1980), Geochemical classification of terrigenous sands and shales from core or log data, *Journal of Sedimentary Research*. **58**(5): 820-829. doi:10.1306/212F8E77-2B24-11D7-8648000102C1865D.
- Hoskin PW and Black LP (2002), Metamorphic zircon formation by solid-state recrystallization of protolith igneous zircon, *Journal of metamorphic Geology*. **18**(4): 423-39.
- Hossain I, Tsunogae T and Rajesh HM (2009), Geothermobarometry and fluid inclusions of dioritic rocks in Bangladesh: Implications for emplacement depth and exhumation rate, *Journal of Asian Earth Sciences*. **34**(6): 731-739. doi:10.1016/j.jseaes.2008.10.010.
- Hossain I, Tsunogae T, Jannatun N, Rahman MS, Nahar M, Hasan AM and Khatun MM (2023), Mineral compositional constraints on the petrogenesis of gabbroic and monzodioritic rocks in Rangpur District, NW Bangladesh, *Journal of Asian Earth Sciences: X*. **9**: 100134. doi:10.1016/j.jaesx.2022.100134.
- Hossain I, Tsunogae T, Rajesh HM, Chen B and Arakawa Y (2007), Palaeoproterozoic U–Pb SHRIMP zircon age from basement rocks in Bangladesh: A possible remnant of the Columbia supercontinent, *Comptes Rendus Geoscience*. **339**(16): 979-786.
- Hossain I, Tsunogae T, Tsutsumi Y and Takahashi K (2018), Petrology, geochemistry and LA-ICP-MS U-Pb geochronology of Paleoproterozoic basement rocks in Bangladesh: an evaluation of calc-alkaline magmatism and implication for Columbia supercontinent amalgamation, *Journal of Asian Earth Sciences*. **157**: 22-39. <https://doi.org/10.1016/j.jseaes.2017.09.016>
- Hou K, Ma X, Li Y, Liu F and Han D (2019), Genesis of Huoqiu banded iron formation (BIF), southeastern North China Craton, constraints from geochemical and Hf-OS isotopic characteristics, *Journal of Geochemical Exploration*. **197**: 60-69.
- Howladar MF, Al Numankh MA and Faruque MO (2018), An application of Water Quality Index (WQI) and multivariate statistics to evaluate the water quality around Maddhapara Granite Mining Industrial Area, Dinajpur, Bangladesh, *Environmental Systems Research*. **6**: 1-8.
- Islam MS (2009), Geological aspects of soil formation of Bangladesh. Alam MJ, In *Geological Aspects of Soil Formation of Bangladesh Conference Paper*, Dhaka, Bangladesh.
- Jones HC (1934), The iron ore deposits of Bihar and Orissa. *Mem. Geol. Surv. India*, **63**: 167-302.
- Kato Y, Ohta I, Tsunematsu T, Watanabe Y, Isozaki Y, Maruyama S and Imai N (1998), Rare earth element variations in mid-Archean banded iron formations: Implications for the chemistry of ocean and continent and plate tectonics. *Geochimica et Cosmochimica Acta*. **62**(21-22): 3475-3497. doi:10.1016/S0016-7037(98)00253-1.
- Klein C (2005) Some Precambrian banded iron-formations (BIFs) from around the world: Their age, geologic setting, mineralogy, metamorphism, geochemistry, and origins, *American Mineralogist*. **90**(10): 1473-1499. doi:10.2138/am.2005.1871.
- Klein C and Beukes NJ (1989), Geochemistry and sedimentology of a facies transition from limestone to iron-formation deposition in the early Proterozoic Transvaal Supergroup, South Africa, *Economic Geology*. **84**(7): 1733-7174.

- Konhauser KO, Planavsky NJ, Hardisty DS, Robbins LJ, Warchola TJ, Haugaard R, Lalonde SV, Partin CA, Oonk PB, Tsikos H and Lyons TW (2017), Iron formations: A global record of Neoproterozoic to Palaeoproterozoic environmental history, *Earth-Science Reviews*. **172**: 140-177. doi:10.1016/j.earscirev.2017.06.012.
- Kucha H (1980), Continuity in the monazite-huttonite series, *Mineralogical Magazine*. **43**(332): 1031-1033. doi:10.1180/minmag.1980.043.332.12.
- Lambeck A (2012). Basin analysis and the geochemical signature of Paleoproterozoic sedimentary successions in northern Australia: constraints on basin development in respect to mineralisation and paleoreconstruction models, Ph.D. Thesis, University of Adelaide, Australia.
- Lan TG, Fan HR, Santosh M, Hu FF, Yang KF and Liu Y (2014), U–Pb zircon chronology, geochemistry and isotopes of the Changyi banded iron formation in the eastern Shandong Province: constraints on BIF genesis and implications for Paleoproterozoic tectonic evolution of the North China Craton, *Ore Geology Reviews*. **56**: 472-486. <https://doi.org/10.1016/j.oregeorev.2013.06.008>
- Lascelles DF (2007), Black smokers and density currents: a uniformitarian model for the genesis of banded iron-formations, *Ore Geology Reviews*. **32**(1-2): 381-411. <https://doi.org/10.1016/j.oregeorev.2006.11.005>
- Lepage LD (2003), ILMAT: an Excel worksheet for ilmenite–magnetite geothermometry and geobarometry, *Computers & Geosciences*. **29**(5): 673-678.
- Li Z, Zhang L, Xue C, Zhu M, Zheng M, Robbins LJ and Konhauser KO (2019), Genesis of the Neoproterozoic–Early Cambrian banded iron ore-bearing sedimentary rocks in the Jierteke-Zankan iron ore belt, West Kunlun Orogenic Belt, Xinjiang (NW China), *Journal of Asian Earth Sciences*. **173**: 143-160. doi:10.1016/j.jseae.2019.01.020.
- Linnen RL and Keppler H (2002), Melt composition control of Zr/Hf fractionation in magmatic processes, *Geochimica et Cosmochimica Acta*. **66**(18): 3293-3301.
- Lipman PW (1971), Iron-titanium oxide phenocrysts in compositionally zoned ash-flow sheets from southern Nevada, *The Journal of Geology*. **79**(4): 438-546. doi:10.1086/627651.
- Liu L, Zhang L and Dai Y (2014), Formation age and genesis of the banded iron formations from the Guyang Greenstone Belt, Western North China Craton, *Ore Geology Reviews*. **63**: 388-404. <https://doi.org/10.1016/j.oregeorev.2013.10.011>
- Liu L, Zhang LC, Dai YP, Wang CL and Li ZQ (2012), Formation age, geochemical signatures and geological significance of the Sanheming BIF-type iron deposit in the Guyang greenstone belt, Inner Mongolia, *Acta Petrologica Sinica*. **28**(11): 3623-3637.
- Manikyamba C, Balaram V and Naqvi SM (1993), Geochemical signatures of polygenetic origin of a banded iron formation (BIF) of the Archaean Sandur greenstone belt (schist belt) Karnataka nucleus, India, *Precambrian Research*. **61**(1-2): 137-164. [https://doi.org/10.1016/0301-9268\(93\)90061-6](https://doi.org/10.1016/0301-9268(93)90061-6)
- Marchig V, Gundlach H, Möller P and Schley F (1982), Some geochemical indicators for discrimination between diagenetic and hydrothermal metalliferous sediments, *Marine Geology*. **50**(3): 241-256. [https://doi.org/10.1016/0025-3227\(82\)90141-4](https://doi.org/10.1016/0025-3227(82)90141-4)
- Miah I, Arefin KM and Arifuzzaman M (2002), Prospect of Metallic Minerals in Madhyapara Hard Rocks: A Geoelectrical Analysis, *Bangladesh J. Geol.* **21**: 1-7.
- Mloszewska AM, Pecoits E, Cates NL, Mojzsis SJ, O'Neil J, Robbins LJ and Konhauser KO (2012), The composition of Earth's oldest iron formations: the Nuvvuagittuq Supracrustal Belt (Québec, Canada), *Earth and Planetary Science Letters*. **317**: 331-342. doi:10.1016/j.epsl.2011.11.020.
- Molnar P and Tapponnier P (1977), The collision between India and Eurasia, *Scientific American*. **236**(4): 30-41.
- Molnar P and Tapponnier P (1975), Cenozoic Tectonics of Asia: Effects of a Continental Collision: Features of recent continental tectonics in Asia can be interpreted as results of the India-Eurasia collision, *Science*. **189**(4201): 419-426.
- Nakayama K and Nakamura T (2005), X-ray fluorescence analysis of rare earth elements in rocks using low dilution glass beads, *Analytical Sciences*. **21**(7): 815-222. <https://doi.org/10.2116/analsci.21.815>
- Ndime EN, Ganno S and Nzenti JP (2019), Geochemistry and Pb–Pb geochronology of the Neoproterozoic West metamorphosed banded iron formation, south-

- ern Cameroon, *International Journal of Earth Sciences*. **108**: 1551-1570.
- Orton GJ and Reading HG (1993), Variability of deltaic processes in terms of sediment supply, with particular emphasis on grain size, *Sedimentology*. **40**(3): 475-512.
- Pecoits E, Gingras MK, Barley ME, Kappler A, Posth NR and Konhauser KO (2009), Petrography and geochemistry of the Dales Gorge banded iron formation: Paragenetic sequence, source and implications for palaeo-ocean chemistry, *Precambrian Research*. **172**(1-2): 163-187. <https://doi.org/10.1016/j.precamres.2009.03.014>
- Peng Z, Wang C, Tong X, Zhang L and Zhang B (2018), Element geochemistry and neodymium isotope systematics of the Neoproterozoic banded iron formations in the Qingyuan greenstone belt, North China Craton, *Ore Geology Reviews*. **102**: 562-584.
- Posth NR, Köhler I, Swanner ED, Schröder C, Wellmann E, Binder B, Konhauser KO, Neumann U, Berthold C, Nowak M and Kappler A (2013), Simulating Precambrian banded iron formation diagenesis, *Chemical Geology*. **362**: 66-73. <https://doi.org/10.1016/j.chemgeo.2013.05.031>
- Pyle JM, Spear FS, Rudnick RL and McDonough WF (2001), Monazite-xenotime-garnet equilibrium in metapelites and a new monazite-garnet thermometer, *Journal of Petrology*. **42**(11): 2083-2107. doi:10.1093/ptrology/42.11.2083.
- Rahman A, Tardio J, Bhargava SK, Zaman MN, Hasan AM, Torpy A and Pownceby MI (2020), Comparison of the chemistry and mineralogy of ilmenite concentrates sourced from fluvial (Brahmaputra River) and beach placer (Cox's Bazar) deposits, Bangladesh, *Ore Geology Reviews*. **117**: 103271. doi:10.1016/j.oregeorev.2019.103271.
- Rao DS and Sengupta D (2014), Electron microscopic studies of ilmenite from the Chhatrapur coast, Odisha, India, and their implications in processing, *Journal of Geochemistry*. doi:10.1155/2014/192639.
- Rao TG and Naqvi SM (1995), Geochemistry, depositional environment and tectonic setting of the BIF's of the Late Archaean Chitradurga Schist Belt, India, *Chemical Geology*. **121**(1-4): 217-43.
- Ray JS, Pattanayak SK and Pande K (2005), Rapid emplacement of the Kerguelen plume-related Sylhet Traps, eastern India: Evidence from ⁴⁰Ar-³⁹Ar geochronology, *Geophysical Research Letters*. **32**: 10.
- Reynolds IM (1983), The Iron-Titanium Oxide Mineralogy of Karoo Dolerite in the Eastern Cape and Southern Orange Free State, Trans. Geol. Soc. South Africa. **86**: 211-220.
- Rubatto D (2002), Zircon trace element geochemistry: partitioning with garnet and the link between U-Pb ages and metamorphism, *Chemical geology*. **184**(1-2): 123-138.
- Sawka WN (1988), REE and Trace Element Variations in Accessory Minerals and Hornblende from the Strongly Zoned McMurry Meadows Pluton, California, *Earth Environ. Sci. Trans. R. Soc. Edinburgh* **79**: 157-168. DOI: <https://doi.org/10.1017/S0263593300014188>
- Schandl ES and Gorton MP (2004), A textural and geochemical guide to the identification of hydrothermal monazite: criteria for selection of samples for dating epigenetic hydrothermal ore deposits, *Economic Geology*. **99**(5): 1027-1035. <https://doi.org/10.2113/gsecongeo.99.5.1027>
- Smith AJ, Beukes NJ and Gutzmer J (2013), The composition and depositional environments of Mesoproterozoic iron formations of the West Rand Group of the Witwatersrand Supergroup, South Africa, *Economic Geology*. **108**(1): 111-34. <https://doi.org/10.2113/econgeo.108.1.111>
- Sun J, Zhu X and Li Z (2018), Confirmation and global significance of a large-scale early Neoproterozoic banded iron formation on Hainan Island, China, *Precambrian Research*. **307**: 82-92. <https://doi.org/10.1016/j.precamres.2018.01.005>
- Sylvestre G, Laure NT, Djibril KN, Arlette DS, Cyriel M, Timoléon N and Paul NJ (2017), A mixed seawater and hydrothermal origin of superior-type banded iron formation (BIF)-hosted Kouambo iron deposit, Palaeoproterozoic Nyong series, Southwestern Cameroon: constraints from petrography and geochemistry, *Ore Geology Reviews*. **80**: 860-875. <https://doi.org/10.1016/j.oregeorev.2016.08.021>
- Sylvestre G, Timoleon N, Djibril KN, Paul NJ and Marianne NF (2015), Petrology and geochemistry of the banded iron-formations from Ntem complex greenstones belt, Elom area, Southern Cameroon: implications for the origin and depositional environment, *Geochemistry*. **75**(3): 375-387. doi:10.1016/j.chemer.2015.08.001.

- Talwani M, Desa MA, Ismaiel M and Sree Krishna K (2016), The tectonic origin of the Bay of Bengal and Bangladesh, *Journal of Geophysical Research: Solid Earth*. **121**(7): 4836-4851.
- Tamehe LS, Tankwa MN, Chongtao W, Ganno S, Ngnotue T, Nono GD, Simon SJ, Zhang J and Nzenti JP (2018), Geology and geochemical constrains on the origin and depositional setting of the Kpwa–Atog Boga banded iron formations (BIFs), northwestern Congo craton, southern Cameroon, *Ore Geology Reviews*. **95**: 620-638.
- Tamehe LS, Wei C, Ganno S, Rosière CA, Nzenti JP, Ebotehouna CG and Lu G (2021), Depositional age and tectonic environment of the Gouap banded iron formations from the Nyong group, SW Cameroon: Insights from isotopic, geochemical and geochronological studies of drillcore samples, *Geoscience Frontiers*. **12**(2): 549-572. doi:10.1016/j.gsf.2020.07.009.
- Taner MF and Chemam M (2015), Algoma-type banded iron formation (BIF), Abitibi Greenstone belt, Quebec, Canada, *Ore geology reviews*. **1**(70): 31-46.
- Tarney J (1976), Geochemistry of archaean high-grade gneisses, with implications as to the origin and evolution of the precambrian crust.
- Teutsong T, Bontognali TR, Ndjigui PD, Vrijmoed JC, Teagle D, Cooper M and Vance D (2017), Petrography and geochemistry of the Mesoarchean Bikoula banded iron formation in the Ntem complex (Congo craton), Southern Cameroon: implications for its origin, *Ore Geology Reviews*. **80**: 267-288.
- Vandenbergh RE, De Resende VG, da Costa GM and De Grave E (2010), Study of loss-on-ignition anomalies found in ashes from combustion of iron-rich coal, *Fuel*. **89**(9): 2405-2410. doi:10.1016/j.fuel.2010.01.022.
- Viehmann S, Bau M, Hoffmann JE and Münker C (2015), Geochemistry of the Krivoy Rog Banded Iron Formation, Ukraine, and the impact of peak episodes of increased global magmatic activity on the trace element composition of Precambrian seawater, *Precambrian Research*. **270**: 165-80.
- Wang C, Konhauser KO and Zhang L (2015), Depositional environment of the Paleoproterozoic Yuanjiacun banded iron formation in Shanxi Province, China, *Economic Geology*. **110**(6): 1515-1539.
- Wark DA and Miller CF (1993), Accessory mineral behavior during differentiation of a granite suite: monazite, xenotime and zircon in the Sweetwater Wash pluton, southeastern California, USA, *Chemical Geology*. **110**(1-3): 49-67.
- Williams ML, Jercinovic MJ and Hetherington CJ (2007), Microprobe monazite geochronology: understanding geologic processes by integrating composition and chronology, *Annu. Rev. Earth Planet. Sci.* **35**: 137-175. doi:10.1146/annurev.earth.35.031306.140228.
- Winter OD (2001), An Introduction to Igneous and Metamorphic Petrology; United States of America. ISBN 0132403420.
- Wu LG, Li XH, Ling XX, Yang YH, Li CF, Li YL, Mao Q, Li QL and Putlitz B (2019), Further characterization of the RW-1 monazite: a new working reference material for oxygen and neodymium isotopic microanalysis, *Minerals*. **9**(10): 583. doi:10.3390/min9100583.
- Zhai M and Santosh M (2013), Metallogeny of the North China Craton: link with secular changes in the evolving Earth, *Gondwana Research*. **24**(1): 275-297. doi:10.1016/j.gr.2013.02.007.
- Zhai MG and Santosh M (2011), The early Precambrian odyssey of the North China Craton: a synoptic overview, *Gondwana Research*. **20**(1): 6-25. doi:10.1016/j.gr.2011.02.005.
- Zhang L, Zhai M, Zhang X, Xiang P, Dai Y, Wang C and Pirajno F (2012), Formation age and tectonic setting of the Shirengou Neoproterozoic banded iron deposit in eastern Hebei Province: constraints from geochemistry and SIMS zircon U–Pb dating, *Precambrian Research*. **222**: 325-338.
- Zhang X, Zhang L, Xiang P, Wan BO and Pirajno F (2011), Zircon U–Pb age, Hf isotopes and geochemistry of Shuichang Algoma-type banded iron-formation, North China Craton: constraints on the ore-forming age and tectonic setting, *Gondwana Research*. **20**(1): 137-148., doi:10.1016/j.gr.2011.02.008.